



MODELLING OF AERODYNAMIC INTERACTIONS IN COMPOUND HELICOPTERS

Carlos Santos Sousa

Dissertaçāo para obtençāo do Grau de Mestre em
Engenharia Aeroespacial

Júri

Presidente: Professor Fernando José Parracho Lau

Orientador: Professor Filipe Szolnoky Ramos Pinto Cunha

Vogais: Professor João Manuel Melo de Sousa

October 2010

ACKNOWLEDGEMENTS

The author would like to thank Prof. Afzal Suleman, Prof. Fernando Lau and Prof. Richard E. Brown for building the bridge between the Instituto Superior Técnico – Universidade Técnica de Lisboa and the University of Glasgow and for conceding him the opportunity to develop his thesis in the later institution. The author is particularly and deeply indebted to Professor Richard E. Brown for all his support and advice and for allowing the author to make use of the data obtained with the VTM computer programme.

The author would like to express his gratitude towards Prof. Karthikeyan Duraisamy for the many things he taught him that extend far beyond the CFD lectures and for all his support during the early stages of the development of this thesis.

The author is very grateful to his colleagues that shared the space of the former Rotor Aeromechanics Laboratory at the University of Glasgow. In particular the author wishes to thank his office companion and bosom friend, Dr. Sébastien Mounoury, for his sharp humour that always brimmed the laboratory with life, Dr. Hyo Won Kim for his cooperation and assistance in collecting and treating the data presented in this thesis and for his stoical patience in helping the author to learn how to interpret the data from the VTM programme, Dr. Adam Kenyon for his genuine interest in getting the author involved in the enhancement of the airframe geometry and for providing the fuselage data presented in this thesis, Dr. Alasdair Thom for his estimable collaboration during preliminary investigations, Dr. Mary Kelly, Dr. Timothy Fletcher and Dr. Catriona Phillips for their invaluable support and friendship and Dr. Gary Ahlin for his helpful advice.

The author wishes to acknowledge Prof. Filipe Cunha for co-orienting his work and for his important role at later stages of the development of this thesis.

The author would like to thank the unconditional support of his family that always offered him the best advice. Finally and above all, the author wishes to thank his girlfriend, Maria Inês, for trusting him so much, for offering her care and patience and for indefatigably raising his spirit in the most difficult moments and injecting him the extra motivation required to finish this thesis.

ABSTRACT

The prediction of aerodynamic interactions has been shown to earn careful consideration in helicopter design because of their consequences to the handling qualities, dynamics and performance. Under forward flight condition at moderate advance ratio, aerodynamic interactions may manifest as high levels of vibration and noise or as large nose-up pitching moments acting on the helicopter. These effects are investigated in a generic coaxial helicopter that is representative of modern configurations and features a hingeless hub, rigid blades and thrust compounding. The correct prediction of the detailed evolution of the vortex structures within the helicopter rotor wake is essential for the analysis of aerodynamic interactions. This is properly addressed by using lifting-line theory coupled to a Vorticity Transport Model to compute the evolution of the vorticity generated at the rotor blades. This finite volume boundary-free model solves the vorticity equation and circumvents the excessive numerical diffusion of vorticity that limits standard CFD-based techniques. Numerical simulations on several combinations of the components that constitute the helicopter were carried out and compared against the results for the full helicopter in order to better understand the origins and effects of the interactional phenomena. It is shown that the effects of some aerodynamic interactions can be directly ascribed to a particular event, like the impingement of the main rotor wake into another component, while others may manifest in a more subtle way, like the mutual interaction between the wakes generated by different rotors or the displacement of the main rotor wake caused by the airframe.

Keywords

Interactional aerodynamics, forward flight, compound helicopter, coaxial rotor, Advancing Blade Concept, Vorticity Transport Model.

RESUMO

A simulação de interacções aerodinâmicas merece grande consideração no projecto de helicópteros devido às suas consequências para a qualidade de voo, dinâmica e performance. Em condição de voo nivelado a razão de avanço moderada, as interacções aerodinâmicas podem manifestar-se como níveis de vibração e ruído elevados ou momentos de cabragem severos aplicados no helicóptero. Estes efeitos são investigados num helicóptero coaxial genérico, composto em propulsão e representativo de configurações modernas caracterizadas por hélices de pás rígidas desarticuladas. A correcta previsão da evolução das estruturas de vórtice que dominam a esteira da hélice do helicóptero é essencial para a análise de interferências aerodinâmicas. Isto é conseguido através da teoria de linha sustentadora em conjunto com o método ‘Vorticity Transport Model’ que são usados para calcular a evolução de vorticidade produzida pelas pás das hélices. Este modelo de volume finito e fronteira-livre resolve a equação de vorticidade, contornando a excessiva difusão numérica que limita as técnicas convencionais de CFD. Simulações numéricas de várias combinações de componentes do helicóptero foram efectuadas e comparadas com os resultados obtidos para a configuração completa de modo a melhor entender as origens e efeitos dos fenómenos de interferência. É demonstrado que os efeitos de algumas interacções aerodinâmicas podem ser directamente imputados a um dado evento, como o embate da esteira da hélice principal num outro componente, enquanto outros podem manifestar-se de um modo mais subtil, como a interacção mútua entre as esteiras produzidas por diferentes hélices ou a deformação da esteira da hélice principal causada pela fuselagem.

Palavras-chave

Interacções aerodinâmicas, Voo rectilíneo uniforme, helicóptero composto, rotor coaxial, Advancing Blade Concept, Vorticity Transport Model.

CONTENTS

List of Tables	vi
List of Figures	vii
Acronyms	xiii
1 Introduction	1
1.1 Historical Perspective	1
1.2 Compound Helicopters	5
1.3 The Advancing Blade Concept	5
1.4 Interactional Aerodynamics and Its Modelling	6
1.5 Objectives	8
1.6 Thesis Layout	8
2 Description of the Simulation Model	11
2.1 Helicopter Geometry	11
2.2 Main Rotor System	12
2.3 Fuselage and Tailplane	14
2.4 Auxiliary Propulsor	16
2.5 Vorticity Equation	17
2.6 Velocity Field	20
2.7 Blade Aerodynamic Model	21
2.8 Trim Model	23
3 Validation of the VTM Computer Programme	26

4 Results	31
4.1 Wake Structure	31
4.2 Isolated Coaxial Rotor	36
4.3 Coaxial Rotor with Auxiliary Propulsor	41
4.4 Complete Configuration	46
5 Conclusion	55
Bibliography	61
A Appendix	65
A.1 Rotorcraft Performance Characteristics	65
A.2 Isolated Main Rotor	66
A.3 Isolated Auxiliary Propulsor	70
A.4 Main Rotor and Auxiliary Propulsor	71
A.5 Complete Configuration	78
A.6 Auxiliary Propulsor Wake	85
A.7 Mean and Root Mean Square Decomposition	86

LIST OF TABLES

2.1	Main rotor and propulsor characteristics	13
2.2	Fuselage geometric properties	15
3.1	Properties of Harrington's rotor 1	28
A.1	Performance characteristics of the isolated main rotor.	65
A.2	Performance characteristics of the main rotor and propulsor configuration.	65
A.3	Performance characteristics of the full configuration.	65

LIST OF FIGURES

1.1	The Sikorsky's XH-59A Advancing Blade Concept Technology Demonstrator Helicopter.	3
1.2	The Sikorsky's X2 Technology Demonstrator. Top Left: concept model. Top Right: flight testing in August 2008. Bottom: flight testing in September 2010. (<i>Courtesy of Sikorsky Aircraft Corp.</i>)	4
1.3	Comparison of the lift distribution and rotor rolling moments for a conventional and ABC rotor system.	6
2.1	Geometry of the simulation model including a generic ABC-type coaxial rotor and a tail propulsor.	11
2.2	Comparison between the velocity field induced by the Biot-Savart kernel and by the Rosenhead-Moore kernel.	20
3.1	Comparison of the overall power consumption with advance ratio in forward flight between the VTM simulations and Dingeldein's experimental data. (Adapted from Ref. [1].)	29
3.2	Comparison of the overall power consumption with advance ratio in forward flight between the VTM simulations and Dingeldein's experimental data using the corrected drag model. (Adapted from Ref. [2].)	30
4.1	Three-dimensional view of the tip vortex filaments trailed by two blades of the coaxial rotor system as given by the prescribed wake model.	32
4.2	Tip vortex filaments trailed by the coaxial rotor system as viewed from above.	32

4.3	Iso-surfaces of vorticity magnitude generated by the main rotor operating in isolation at advance ratio $\mu = 0.15$. (Iso-surfaces from different rotors rendered separately in distinct colours.)	33
4.4	Iso-surfaces of vorticity magnitude generated by the main rotor and propulsor at advance ratio $\mu = 0.15$. (Iso-surfaces from different rotors rendered separately in distinct colours)	34
4.5	Iso-surfaces of vorticity magnitude of the full helicopter configuration at advance ratio $\mu = 0.15$. (Iso-surfaces from different components rendered separately in distinct colours)	35
4.6	Iso-surfaces of vorticity magnitude showing the close-passage of the tip vortices from the main rotor on the upper surface of the tailplane and the ingestion of these vortices by the propulsor.	36
4.7	Distribution of inflow over the blades of the upper and lower rotors during a complete rotor revolution. Left: upper rotor. Right: lower rotor.	37
4.8	Contour plot of the y -component of non-dimensional vorticity (normalized by its maximum value ζ_{max}) in the $x - z$ plane for the isolated main rotor. Region of $ \zeta_y/\zeta_{max} < 0.06$ not plotted for clarity.	37
4.9	Distribution of loading over the blades of the upper and lower rotors during a complete rotor revolution. Left: upper rotor. Right: lower rotor.	38
4.10	Thrust coefficient generated by the upper and lower rotors of the coaxial system as a function of azimuth and respective frequency spectrum.	39
4.11	Comparison between the thrust coefficient generated by the upper rotor obtained with the VMT and the UIM simulations and respective frequency spectrum.	40
4.12	Contour plot of the y -component of non-dimensional vorticity (normalized by its maximum value ζ_{max}) in the $x - z$ plane for the configuration composed of the main rotor and auxiliary propulsor. Region of $ \zeta_y/\zeta_{max} < 0.06$ not plotted for clarity.	41

4.13 Distribution of loading over the blades of the upper and lower rotors during a complete rotor revolution for the configuration comprised of the main rotor and auxiliary propulsor. Left: upper rotor. Right: lower rotor.	42
4.14 Distribution of inflow over the blades of the auxiliary propulsor as seen from behind the helicopter when operating together with the main rotor. Left: mean inflow. Right: RMS fluctuation in inflow.	44
4.15 Distribution of blade loading over a representative blade of the auxiliary propulsor as seen from behind the helicopter when operating together with the main rotor. Left: mean loading. Right: RMS fluctuation in loading.	44
4.16 Thrust coefficient generated by the auxiliary propulsor over a complete main rotor revolution as a function of main rotor azimuth and respective frequency spectrum. (Thrust coefficient defined on the basis of the rotational speed, Ω_p , and radius, R_p , of the auxiliary propulsor.	45
4.17 Contour plot of the y -component of non-dimensional vorticity (normalized by its maximum value ζ_{max}) in the $x-z$ plane for the complete configuration. Region of $ \zeta_y/\zeta_{max} < 0.06$ not plotted for clarity.	46
4.18 Distribution of the difference in inflow between the complete configuration and that comprised of the main rotor and auxiliary propulsor. Left: upper rotor. Right: lower rotor.	47
4.19 Distribution of the difference in blade loading between the complete configuration and that comprised of the main rotor and auxiliary propulsor. Left: upper rotor. Right: lower rotor.	48
4.20 Thrust coefficient generated by the upper and lower rotors of the coaxial system as a function of azimuth and respective frequency spectrum for the complete configuration.	49
4.21 Distribution of blade loading over a representative blade of the auxiliary propulsor as seen from behind for the complete configuration. Left: mean loading. Right: RMS fluctuation in loading.	51

4.22 Thrust coefficient generated by the auxiliary propulsor over a complete main rotor revolution as a function of main rotor azimuth and respective frequency spectrum for the complete configuration. (Thrust coefficient defined on the basis of the rotational speed, Ω_p , and radius, R_p , of the auxiliary propulsor.	51
4.23 Variation of the time averaged pressure coefficient along the top centreline of the fuselage. (Error bars represent the amplitude of the RMS fluctuations in the pressure signal obtained for the full configuration. <i>Courtesy of Dr. H. Kim and Dr. A. Kenyon.</i>)	52
4.24 Contours of the unsteady pressure component along the top centreline as a function of main rotor azimuth obtained for the full configuration. Mean component of the signal removed. (<i>Courtesy of Dr. H. Kim and Dr. A. Kenyon.</i>)	53
A.1 Tip vortex filaments trailed by the coaxial rotor system as viewed from above. Lower rotor rotating with $\pi/3$ rad in advance with respect to the upper rotor.	
A.1	66
A.2 Tip vortex filaments trailed by the coaxial rotor system as viewed from above. Lower rotor rotating with $\pi/2$ rad in advance with respect to the upper rotor.	
A.2	66
A.3 Bottom view of the iso-surfaces of vorticity magnitude generated by the main rotor when operating in isolation at advance ratio $\mu = 0.15$. (Iso-surfaces from different rotors rendered separately in distinct colours.)	
A.3	67
A.4 Power coefficient consumed by the upper and lower rotors of the main coaxial system and correspondent frequency spectrum for the isolated main rotor.	
A.4	68
A.5 Pitching moment coefficient produced by the upper and lower rotors of the main coaxial system and correspondent frequency spectrum.	
A.5	69
A.6 Distribution of blade loading over a representative blade of the auxiliary propulsor during a complete revolution when the auxiliary propulsor is operating in isolation and producing the same thrust as when operating in the full configuration. Left: mean loading. Right: RMS fluctuation in loading.	
A.6	70

A.7	Distribution of blade loading over a representative blade of the auxiliary propulsor during a complete revolution when the auxiliary propulsor is operating in isolation with the same collective pitch control as when operating in the full configuration. Left: mean loading. Right: RMS fluctuation in loading.	70
A.8	Bottom view of the iso-surfaces of vorticity magnitude generated by the main rotor when operating together with the auxiliary propulsor at advance ratio $\mu = 0.15$. (Iso-surfaces from different rotors rendered separately in distinct colours.)	71
A.9	Distribution of inflow over the blades of the upper and lower rotors during a complete rotor revolution for the configuration comprised of the main rotor and auxiliary propulsor. Left: upper rotor. Right: lower rotor.	72
A.10	Thrust coefficient generated by the upper and lower rotors and correspondent frequency spectrum for the configuration comprised of the main rotor and auxiliary propulsor.	73
A.11	Power coefficient consumed by the upper and lower rotors and correspondent frequency spectrum for the configuration comprised of the main rotor and auxiliary propulsor.	74
A.12	Pitching moment coefficient produced by the upper and lower rotors and correspondent frequency spectrum for the configuration comprised of the main rotor and auxiliary propulsor.	75
A.13	Power coefficient consumed by the auxiliary propulsor over a complete main rotor revolution as a function of main rotor azimuth and respective frequency spectrum. (Power coefficient defined on the basis of the rotational speed, Ω_p , and radius, R_p , of the auxiliary propulsor.	76
A.14	Pitching moment coefficient generated by the auxiliary propulsor over a complete main rotor revolution as a function of main rotor azimuth and respective frequency spectrum. (Pitching moment coefficient defined on the basis of the rotational speed, Ω_p , and radius, R_p , of the auxiliary propulsor.	77

A.15 Bottom view of the iso-surfaces of vorticity magnitude generated by the main rotor as part of the complete configuration at advance ratio $\mu = 0.15$. (Iso-surfaces from different rotors rendered separately in distinct colours.)	78
A.16 Distribution of inflow over the blades of the upper and lower rotors during one rotor revolution for the complete configuration. Left: upper rotor. Right: lower rotor.	79
A.17 Distribution of loading over the blades of the upper and lower rotors during one rotor revolution for the complete configuration. Left: upper rotor. Right: lower rotor.	80
A.18 Power coefficient consumed by the upper and lower rotors and correspondent frequency spectrum for the complete configuration.	81
A.19 Pitching moment coefficient produced by the upper and lower rotors and correspondent frequency spectrum for the complete configuration.	82
A.20 Power coefficient consumed by the auxiliary propulsor over a complete main rotor revolution as a function of main rotor azimuth and respective frequency spectrum, for the complete configuration. (Power coefficient defined on the basis of the rotational speed, Ω_p , and radius, R_p , of the auxiliary propulsor.	83
A.21 Pitching moment coefficient generated by the auxiliary propulsor over a complete main rotor revolution as a function of main rotor azimuth and respective frequency spectrum for the complete configuration. (Pitching moment coefficient defined on the basis of the rotational speed, Ω_p , and radius, R_p , of the auxiliary propulsor.	84
A.22 Contour plot of the y -component of non-dimensional vorticity in the $x - z$ plane that is produced by the auxiliary propulsor. a) Isolated auxiliary propulsor. b) Auxiliary propulsor operating under the influence of the main rotor wake. c) Auxiliary propulsor operating under the influence of the main rotor wake, fuselage and tailplane.	85

ACRONYMS

ABC Advancing Blade Concept

BVI Blade-Vortex Interaction

CFD Computational Fluid Dynamics

HSI High Speed Interaction

LSI Low Speed Interaction

RMS Root Mean Square

ROBIN ROtor Body INteraction

UIM Uniform Inflow Model

VTM Vortex Transport Model

1 INTRODUCTION

1.1 Historical Perspective

Since time immemorial, mankind has been dreaming of flying with unconstrained freedom together with full motion control. Since early days, man has been striven after a reliable and practical machine that could raise him to the skies, fly in any commanded direction and then come down again to the ground in a comfortable and safe journey. The helicopter, as we know it today, is by far the flying vehicle that more closely satisfies that demand due to its inherent flying characteristics – its ability to take-off and land vertically, and to hover for extended periods of time, as well as its handling properties under low airspeed conditions. This idea is well patent in the following citation from Igor Sikorsky,

“The helicopter approaches closer than any other [vehicle] to fulfillment of mankind’s ancient dreams of the flying horse and the magic carpet.”

The first recorded attempt to build a vertical flight machine stem back to early 1480’s, when the great Italian Leonardo Da Vinci pre-dated the helicopter with a design sketch for a machine that could be described as an “aerial screw”, [3]. However, it was the ancient Chinese flying top that inspired the first helicopter models almost 300 years later, with the first small scale models featuring a pair of coaxial counter-rotating rotors developed by the Russian Mikhail Lomonosov and a few years later by the French Christian De Launoy and his mechanic, Bienvenu.

Although experiments with helicopters appear early in history, its progress was beset by some fundamental technical problems. The aerodynamics of vertical flight were yet to be grappled and the lack of technology to build a suitable engine with higher power-to-weight ratio was not to be overcome until about 1920. By that time, the internal combustion engine allowed for the development of the first full-sized models, but then rotor torque reaction became a major problem. Also, the lack of stability and proper means of control constituted a barrier in the development of the earlier helicopter models. It followed a period of prominent advancements in helicopter design. It was not until 1936 that many of the problems that shattered the hopes of earlier designers were properly addressed, leading to what is considered the first practical fully-con-

trollable helicopter that was successfully flown, the German Focke-Wulf Fw 61. A few years later, in 1942, Igor Sikorsky designed the R-4, which became the first helicopter to reach mass production, [4].

On achievement of practical controlled powered flight, designers became quickly enthralled by the need of improving the performance of the helicopter. Several limitations in the lifting and propulsive capabilities of the single rotor helicopter were encountered in forward flight, namely the adverse effects of compressibility on the advancing blades and stall on the retreating blades, which can be ascribed to the asymmetric flow conditions experienced by the rotor. As the forward speed of the helicopter was increased the difference in dynamic pressure between the advancing and retreating sides of the rotor disk became greater. An increase in the cyclic pitch then needed to be fed to the rotor blades not only to maintain the aircraft in roll trim but also to tilt the disk further forward to overcome the increase in drag of the entire aircraft. Accompanying the increase in cyclic pitch was a reduction in the amount of collective pitch in order to avoid blade stall on the retreating side of the rotor disk, where the collective and cyclic pitch add up to increase blade pitch. That implied a decrease in the rotor thrust capability, leaving rotor designers immersed in a speed trap, [5]. The benefit from the advancing blade lift potential is also compromised as a consequence of the inefficient angles of attack in which the advancing blades operate. An increase in the rotational speed of the rotor will give rise to a higher dynamic pressure which will alleviate the problem of the retreating blade stall, but will expose the advancing blades to the restrictive compressibility effects.

In order to expand the flight envelope of the helicopter, designers needed to overcome the limitations imposed by retreating blade stall and advancing blade compressibility that arose in forward flight. A method to circumvent this limitations was to supplement the helicopter with an additional wing and/or propulsion device, which is commonly known as the compound helicopter. Extensive research has been performed since the end of the Second World War, with many compound helicopter prototypes produced and trialled mainly with the aim of increasing the maximum forward speed of the helicopter. Worth to mention is the British Fairey Gyrodyne first flying on December 1947. On June 1948 the compound Gyrodyne set a world speed record by flying at 200 km/h, although at such high speeds it behaved more like an autogyro rather than a true helicopter. Other notable practical compound helicopters include the Fairey Rotodyne that set the world speed record in the convertiplane category, at 307.2 km/h on January 1959, and Lockheed AH-56A Cheyenne, [6], first flying on September 1967.

Another promising solution to the retreating blade stall and its associated limitations in performance began at Sikorsky Aircraft in 1964, with the Advanc-

ing Blade Concept (ABC) research helicopter. In August 1973 the XH-59A Advancing Blade Concept demonstrator aircraft was flown in order to investigate the ABC rotor characteristics, figure 1.1(a). Unfortunately, an accident occurred in a hard landing after a low speed forward flight test at an altitude of about 15 m. The helicopter pitched nose-up, lost altitude, and hit the ground with its tail, leaving the aircraft extensively damaged. Investigation results disclosed an underprediction of cyclic control requirements at low speed leading to insufficient longitudinal control, [7], rather than a basic flaw in the concept. Another model was built the following year and flight testing commenced in July 1975. In April 1978, tests were conducted with the addition of two pod-mounted 1361 kg thrust Pratt & Whitney J60-P-3A turbojet engines for thrust compounding, further expanding the flight envelope with a top speed of 488 km/h in forward level flight, figure 1.1(b).



(a) XH-59A Advancing Blade Concept technology demonstrator helicopter without auxiliary propulsion.



(b) Second version of the XH-59A compounded in thrust with two J60-P-3A turbojet engines.

Figure 1.1: The Sikorsky's XH-59A Advancing Blade Concept Technology Demonstrator Helicopter.

Later in the 1980's, another project was proposed that implemented the ABC rotor. It was designated the XH-59B and derived from the former XH-59A model through the introduction of several modifications, including a new engine, a shorter fuselage, advanced rotors and a ducted pusher propeller mounted at the tail to provide forward thrust. However, a full-scale model was

never built and the XH-59 programme was abandoned. The advantages of the Advancing Blade Concept were outweighed by the excessively heavy rotor and transmission system and by the very high levels of vibration induced by the rotor system at high speed forward flight. In addition, numerous minor structural concerns were reported and low-speed autorotative yaw control revealed to be unsatisfactory, [8].

Yet the ABC-type coaxial rotor has been brought back recently with the modern Sikorsky's X2 high-speed technology demonstrator, achieving its first flight in August 2008, as depicted in figure 1.2. The X2 was designed to cruise comfortably at 460 km/h while retaining the handling qualities in low-speed flight and the efficiency in hover that are characteristic of the conventional helicopter. The transition to high speed flight is designed to be seamless and simple. During a 1.1 hour flight in the 15th of September 2010, it successfully achieved a speed of 463 km/h true air speed in level flight thus exceeding by 63 km/h the officially recognized top speed for a helicopter – 400 km/h by a Westland Lynx in 1986. The X2 features a LHTEC-T800 engine, a four-bladed coaxial rotor and a six-bladed pusher-type propeller. It also includes fly-by-wire controls and active vibration control that are hoped to circumvent the high levels of vibration that jeopardized the XH-59 programme.



Figure 1.2: The Sikorsky's X2 Technology Demonstrator. Top Left: concept model. Top Right: flight testing in August 2008. Bottom: flight testing in September 2010. (*Courtesy of Sikorsky Aircraft Corp.*)

1.2 Compound Helicopters

A possible solution to the retreating blade problem is to add wings to the fuselage that could share the task of supporting the weight of the aircraft, thus unloading the rotor at high speeds. This is known as lift compounding. Another possible way of augmenting the propulsive force generated by the rotor is by adding a propulsion device, which is known as propulsive thrust compounding. Although lift compounding did not provide a significant increase in forward speed, it could be greatly enhanced with the addition of a propulsion device because the forward disc tilt of the main rotor would no longer be required and the benefits of unloading the main rotor could now be used with plenitude, [5]. This is known as fully compounding. It was the combination of both lift and propulsion compounding that brought helicopter designers up to high speed forward flight.

In the present helicopter model both lift and propulsive thrust compounding were implemented. The former was achieved with the introduction of an extra rotor, arranged in coaxial configuration with the first and rotating in the opposite direction and the latter was accomplished through the addition of a pusher propeller mounted at the rear of the fuselage.

1.3 The Advancing Blade Concept

The ABC helicopter was comprised of a pair of rotors arranged in a coaxial configuration and rotating in opposite directions to each other. The blades were very stiff compared to conventional helicopter blades. They were designed to be particularly stiff under three modes of bending corresponding to three degrees of freedom of blade flexure, namely under flapwise bending (virtual deflection in the direction of blade flap), chordwise bending (direction of blade lag) and torsional bending (direction of blade pitch). The blades were rigidly attached to the hub except for feathering freedom. The concept derives its name from the fact that it makes more efficient use of the lift generated on the advancing blades at high speed forward flight. The advancing blades of each rotor may operate at higher pitch angles to produce more lift without prejudice to roll trim, since the difference in lift between the advancing and retreating sides of the upper rotor are balanced by the equal and opposite lift distribution of the lower blade. Figure 1.3, adapted from the work of Paglino, [9], better illustrates this principle. Rotor lift is then retained with increasing speed and speed capability is maintained at altitude, [8]. In addition, the maximum lift-to-drag ratio (L/D) is improved, [10].

In terms of induced power consumption, the coaxial rotor as proved to be

intrinsically more efficient in hover, forward flight and during manoeuvres than a single rotor of the same solidity and blade geometry, [1]. In addition, the coaxial rotor provides torque cancellation, thereby eliminating the need for a tail rotor and its associated shafting and gearboxes. This turns out to be a prominent feature of the coaxial rotor since in conventional helicopters the tail rotor requires typically 5 to 10% of the main rotor power without making any significant contribution to the thrust generated by the main rotor, [4]. Nonetheless, the advantages of the ABC rotor cannot be summarized to performance benefits, but extend to substantial improvements in handling qualities, acoustics, loads and dynamics compared to contemporary conventional helicopters, [8].

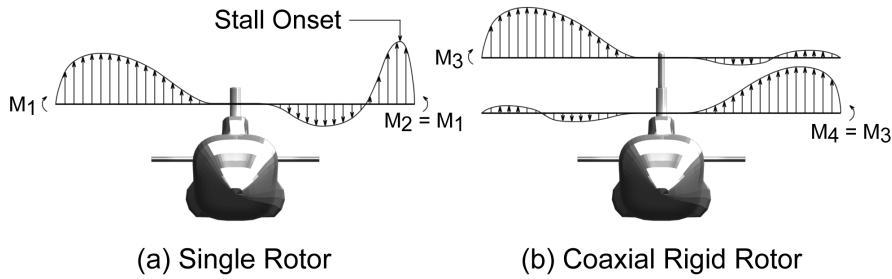


Figure 1.3: Comparison of the lift distribution and rotor rolling moments for a conventional and ABC rotor system.

Since both rotors combine very stiff blades and a hingeless hub, the distance between them was allowed to be minimized in order to reduce parasite drag without the risk of blade tip collision. These rotor characteristics also gave rise to a substantially higher control power than conventional rotors which translated into a faster response to pilot's inputs and ultimately led to an extremely agile, highly manoeuvrable and easier to fly helicopter, [11, 9].

1.4 Interactional Aerodynamics and Its Modelling

Throughout their history, helicopters have progressed at a rather slow pace. Many of the shortcomings that have been reported stem from the intricate interference effects between the surrounding flow field and the various parts that constitute the helicopter. In the vast majority of cases, the complex dynamics of the flow field result in several types of interactions which are highly unsteady in nature and strongly dependent on the particular operational flight condition. They are responsible for a wide range of issues that include a negative impact on performance, unsatisfactory flight dynamics and handling qualities, high blade loading, high vibration and high noise levels.

Extensive research has been conducted to investigate this topic. In 1980, the authoritative work of Sheridan and Smith, [12], provided some good insight to the various forms of possible aerodynamic interactions that take place during helicopter flight. Whilst these interactions are complex and do not occur in isolation, in the sense that all the flow disturbances act on every helicopter component of the helicopter, as well as all the various components act on each of the flow disturbances and these effects combine to give the resultant aerodynamic environment and behaviour of the components, Sheridan and Smith classified the categories of these interactions according to the helicopter components involved and the associated flow anomaly. For instance, the ‘main rotor-fuselage’ interaction referred to the effects induced by the main rotor wake in the fuselage loading and the associated flow anomaly could be of the ‘wake impingement’ type. They also distinguished between the ‘main rotor-fuselage’ and ‘fuselage-main rotor’ types of interactions, for instance, and recognized the mutual effects of both components on each other. The reductive approach of this method provides good insight into the various aerodynamic interactions present within the system and is adopted in this study.

More recently, a study on the main rotor-tail rotor wake interaction and its impact on yaw control developed by Fletcher and Brown, [13], disclosed two distinct modes of interaction between the main rotor and tail rotor that are amenable to be verified whenever a pair of distinct rotors are operating relatively close to each other. The first mode is termed ‘direct’ mode because it is related to the direct effect caused by the wake of one of the rotors that impinges on the other thus subjecting the affected blades to a modified aerodynamic environment that leads to variations in the loading and hence affecting overall performance. The second mode of interaction is the ‘indirect’ mode and consists in the mutual interaction between the wakes of the two rotors. Whilst this second mode of interaction is more subtle than the first, it is often visualized as a distortion of the geometries of both wakes, even at a distance from the intervening rotors. Yet it still has an impact in the blade loads and performance of the rotors because the altered wake geometries feed back into the aerodynamic environment of the rotor system. Both modes of interaction, and specially the second mode, may be better tracked if the wake geometry and loads generated by both rotors in its real configuration are compared against the respective data generated when the rotors are operated in isolation at equivalent flight conditions and trim.

Although much remains to be achieved in the modelling of aerodynamic interactions between the various components of the helicopter, numerical helicopter programs have progressed to a stage where some aspects of these interactions can be modelled to an appreciable degree of realism, [14]. In

particular, those using Computational Fluid Dynamics (CFD) techniques can provide fundamental insight into the structure and geometry of the wakes induced by helicopter rotors because they are based in a very elementary level of description of the helicopter aerodynamics. The Vortex Transport Model (VTM) is one of these techniques, yet it departs somewhat from the standard CFD methodology, in that it simulates the vorticity dominated aerodynamic environment of the helicopter rotor wake directly as a time-dependent vorticity distribution in the space surrounding the helicopter using the vorticity-velocity form of the Navier-Stokes equations, hence allowing more control of the effects of numerical diffusion and dissipation of vorticity, [15]. The present work uses such a model to examine the flow physics that underlie the aerodynamic interactions between the various components of a helicopter with a ABC type coaxial rotor.

1.5 Objectives

The objective of the present thesis is to analyse the aerodynamic environment and blade loads generated by a coaxial helicopter configuration with an auxiliary tail propulsor flying forward at advance ratio $\mu = 0.15$. The rotor system is comprised of two very rigid hingeless rotors as to follow the Advancing Blade Concept rotor systems. This analysis comprises the quantification and characterization of the most significant aerodynamic interactions between the different parts of the helicopter and its influence in the unsteady loads on the blades of the main rotor and tail propulsor.

1.6 Thesis Layout

This section renders a short overview of the structure of this thesis.

Chapter 1 begins with an historical presentation of facts, from the early attempts to develop a vertical flight machine that culminated in the first practical helicopter to the more recent and state-of-the-art X2 Technology Demonstrator, in which the helicopter model of the current work is inspired. This chapter also gives a brief exposition of some of the well-known fundamental technical problems that hampered the progress of the earlier helicopters and motivated the surge of the compound helicopter. Then, it highlights the attributes of the Advancing Blade Concept – a solution that effectively provides lift compounding through the use of a coaxial rotor and, although dating back to the sixties, Ref. [10], continues to attract the interest of the industry. Chapter 1 closes with an insight into the subject of interactional aerodynamics. It focuses on the network-type analysis and associated reductionist approach of Ref. [12]

and offers examples of typical aerodynamic interactions that occur during helicopter flight and have been subject of research. Finally, it introduces the Vorticity Transport Model as an efficient technique for modelling vorticity dominated flows.

Chapter 2 is devoted to the physical and computational details of the model that is the object of this study. The model consists in the helicopter body composed of several distinct components and a computer programme that simulates the evolution of the flow field around the body from an Eulerian perspective. In this chapter, a succinct description of each component is provided and particular attention is given to the description of the coupled lifting-line – VTM concept that constitutes the computer programme used for the simulations. Firstly, the vorticity-velocity formulation is approached with a derivation of the equations in which the VTM concept is grounded. The simplifying assumptions that underlie these equations are exposed in order to better understand the restrictions on the physics that are captured by this method. Secondly, the lifting-line method is introduced as the vehicle for the computation of the shed and trailed vorticity produced by the rotor blades. Emphasis is placed in the way these two concepts are coupled together, with the vorticity being fed into the computational domain through a source term figuring in the aforementioned equations, in one hand, and its convection inside the domain being evolved according to the VTM method in the other hand. This chapter closes with a brief explanation of the methods and simplifying assumptions employed for the trimming of the helicopter model.

Chapter 3 concentrates in the validation of the VTM computer programme. It gathers some references to previous works that used the VTM to predict the flow field around isolated coaxial rotor systems in hover and forward flight. The experiments that were conducted are summarised and the quality of the predictions is reported. This chapter also provides references that give an account of the predictions obtained with the VTM on the pressure distribution over a helicopter fuselage developed for the study of rotor-fuselage interactions.

Chapter 4 presents the results obtained with the coupled lifting-line – VTM method, for steady level flight at advance ratio $\mu = 0.15$. As mentioned before, the helicopter model is divided into different components. In this chapter, results are given with respect to three different combinations of these components, in order to follow the reductionist approach. Each combination forms a helicopter configuration that is analysed in this chapter by order of increasing complexity, namely the isolated coaxial main rotor, the main rotor with auxiliary propulsor and the combined main rotor, auxiliary propulsor, fuselage and tailplane. The first step of this presentation is analysing how the geometry of the vortex structures within the wake of the main rotor depart from an idealized

case where they are not allowed to interact with each other. The next step is understanding how the vortex structures produced by the individual lifting components influence each other and how these wake structures change between the different configurations. After the analysis of the wake structure, the features that characterise the aerodynamic environment of the isolated coaxial rotor are studied and the different aerodynamic interactions between both the upper and lower rotors are identified. Then, the system is allowed to grow in complexity with the inclusion of the auxiliary propulsor and, at a later stage, fuselage and tailplane. The modifications to the inflow velocity and blade loading of the main rotor system as well as their impacts on the performance of the vehicle are investigated. The induced aerodynamic effects caused by the main rotor on the propulsor and fuselage are also analysed.

Finally, chapter 5 closes the current thesis. It begins to point out some possible sources of inaccuracy inherent to the coupled lifting-line – VTM model. Taking that into account, it then draws conclusions based on the results from the current work and gives some suggestions to further the analysis of aerodynamic interactions recurring to this model.

2 DESCRIPTION OF THE SIMULATION MODEL

2.1 Helicopter Geometry

The geometry of the helicopter configuration was purposely made to resemble helicopters like the XH-59A or the X2, while still representing a generic modern ABC-type helicopter configuration, as depicted in figure 2.1. The dimensional and geometric characteristics of the XH-59A main rotor are documented in [16, 17].

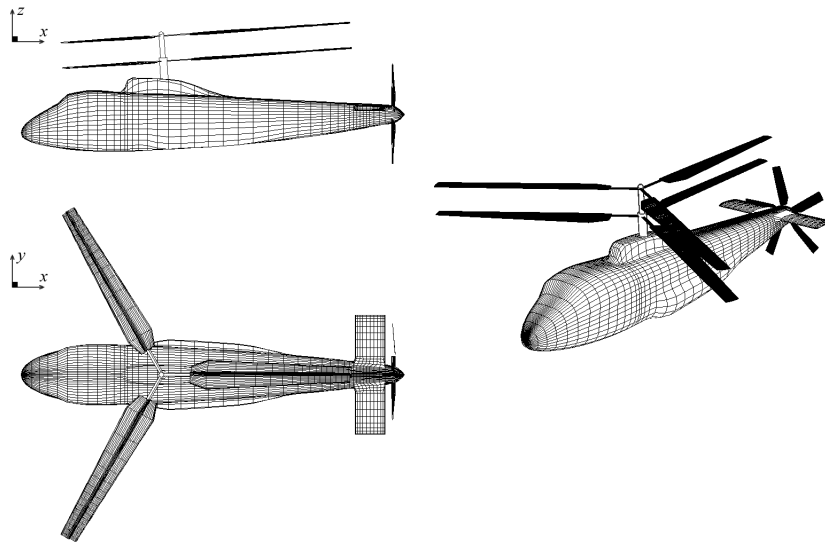


Figure 2.1: Geometry of the simulation model including a generic ABC-type coaxial rotor and a tail propulsor.

Whilst the task of developing a computer geometry that mimics a real helicopter into a high level of detail can be a great challenge to the designer due to the panoply of complex shapes that form many helicopter components in one hand, and in the time constraints in the other hand, a compromise should be reached between design fidelity and practical constraints. These constraints include availability of computer resources, maximum allowed duration for the design phase and suitability to fulfil research aims. Having this in mind, signifi-

cant simplifications have been introduced in the model geometry. Hence, both the main rotor and propulsor hubs are not included in the simulations. However, an entirely fictitious main rotor mast and propulsor hub are included in the drawings, as can be seen in figure 2.1, in order to connect the main rotor and propulsor to the fuselage and thus clarify the relative positions of these components and foster a more realistic impression of the helicopter model. The omission of the hubs in the aerodynamic model may have some obvious effects in the structure of the wake immediately downstream of the rotor shaft. In addition, the blade geometry is not modelled directly, instead it is concealed in the blade aerodynamic model, to be described later in this chapter. However, the blade geometry is indirectly simplified in its aerodynamic model because it relies on two-dimensional airfoil data, thus not incorporating the effects of the three-dimensionality in the flow near the blade surface. Yet, the use of this approach is quite common in comprehensive rotor codes since it still gives a very accurate description of the evolution of the main rotor and propulsor wakes and a reasonably precise representation of the flow field, except perhaps near the surface of blades and wings.

2.2 Main Rotor System

The main rotor consists of two axially aligned rotors. The upper rotor rotates counterclockwise while the lower rotor rotates clockwise, when viewed from above. Each rotor is comprised of three blades and its centres are separated by a distance of $0.139R$, where R stands for main rotor radius. The main rotor has a solidity of 0.127, which is equal to the solidity of the XH-59A rotor system. The blades have linear taper and -10° of non-linear twist. Real ABC-type rotors possess blades with rather complex spanwise variation of airfoil section and twist distribution, [18]. Some even implement distinct airfoil sections at different blade stations. For instance, the Sikorsky XH-59A combined three different types of airfoil sections, the NACA 63(230)-224A, NACA 63(230)-213A and NACA 23012(64), [17].

A departure from these sophisticated rotor designs was adopted, concerning the choice of airfoil sections, in order to simplify the geometry of the blade used in the simulations. Therefore, a NACA 23012 airfoil section was kept constant along the entire span of the main rotor blades. The geometric properties of the main rotor system are summarised in table 2.1. Note that this table also provides data for the auxiliary propulsor, which is introduced in a later section.

The upper rotor is designed to rotate anticlockwise and the lower rotor to rotate clockwise when viewed from above. The phasing of the rotors is arranged such that blades from the upper and lower rotors overlap at an azimuth of 0° .

Note that the azimuth angle, ψ , follows the traditional convention and thus is defined as zero when a blade is pointing downstream.

In terms of structural characteristics, the rotor blades and their attachments to the rotor hub are assumed to be completely rigid. This simplification permits a decoupling of the aerodynamic response of the system from its structural dynamics.

Table 2.1: Main rotor and propulsor characteristics

	Main rotor	Propulsor
Rotor Radius	5.5 m	$0.28R$
Number of rotors	2	1
Blades per rotor	3	5
Root cut-out	$0.12R$	$0.20R_p$
Twist	-10°	-30°
Chord	Tapered (2 : 1)	$0.18R_p$
Airfoil Sections	NACA 23012	NACA 0012

The main rotor blades are modelled computationally according to the Weisinger L-method, which is a modified version of the lifting-line method. This topic is approached briefly in section 2.7.

A study was conducted in order to evaluate the impact of rotor stiffness on the performance of the ABC-type coaxial rotor and to disclose the level of approximation involved in the modelling of a completely rigid rotor configuration to the detriment of the real rotor with flexible, although rather stiff blades, [2]. The study incorporated finite stiffness blades, where the rotor flapwise stiffness was modelled very simply by assuming each rotor blade to be rigid and articulated in flap through the introduction of a hinge at some distance from the rotational axis together with a suitable flap spring. The stiffness of this spring was determined by matching the natural frequency of the blade model with the first flap mode frequency of the flexible blades of a real helicopter. The particular rotor blades that served as a baseline to that study were those of Sikorsky's XH-59A. Since the principal blade modes are known to vary with rotor speed, two test cases were analysed that corresponded to the limiting rotational speeds of operation. Hence, the XH-59A was designed to operate at or near 345 rpm in hover and low speed flight and at values as low as 240 rpm in high speed cruise flight, yielding natural frequencies of the first flap mode of approximately 1.8 cycles/rev and 1.5 cycles/rev respectively, [11, 8]. Then, frequencies of 1.5 and 2 cycles/rev were considered to be representative of a generic ABC-type coaxial system, and computer simulations were conducted at these flap

frequencies and were compared against the completely rigid model. The rotors of all test cases were trimmed to the same thrust, $C_T = 0.0048$, forward force and, in the case of the stiffened rotors, overall moment. The lateral force component was not trimmed in any instance. Three flight conditions were simulated, corresponding to advance ratios of 0.12, 0.24 and 0.36. The auxiliary propulsor was only included at the higher advance ratio. The results pertaining to the time-dependent component of the aerodynamic forces and moments and to the wake geometry of the coaxial system revealed consistent qualitative similarities between the finite stiff coaxial rotors and the rigid coaxial rotor at an advance ratio of 0.12. However, for real systems with flexible blades the relationship between aerodynamic loads and helicopter vibration characteristics departs somewhat from the results obtained in this study because of the simplifying assumptions involved on the dynamic characteristics of the blades themselves. Yet, concerning the effects of aerodynamic interactions, the approximation introduced with the rigid rotor system still yields a close representation of the flow field that is experienced by practical very stiff coaxial rotor systems.

2.3 Fuselage and Tailplane

The geometry of the fuselage was inspired by full-scale helicopter models like the XH-59A or the X2, and tries to represent the compact and streamlined fuselage of modern high-performance helicopters. The fuselage includes two side pods and a tailplane and its length, ℓ , is about two times the main rotor blade radius. A summary of the geometric properties of the fuselage is given in table 2.2.

The fuselage surface is modelled as a set of 2810 discrete panels. Each panel may assume a quadrilateral or triangular shape. The latter is obtained by superposing two vertices of the quadrilateral. Each panel represents a closed loop of vorticity, with each segment forming a vortex filament of constant strength. Then the velocity at the centroid of each panel may be decomposed into two contributions, one is the velocity induced by any vortex filaments and the other is the velocity induced by any other vorticity within the flow, \vec{w} . The vorticity strength of each vortex loop is set to satisfy the boundary condition of zero normal flow across the solid surface and at the centroids of the respective panel. This condition yields the following system of equations,

$$\left(\vec{V}_\infty + \vec{w} \right)_i \cdot \vec{n}_i + \sum_{j=1}^N a_{ij} \Gamma_j = 0, \quad \text{for } i = 1, \dots, N \quad (2.1)$$

where the a_{ij} are known influence coefficients and Γ_j are the vortex loop strengths that are to be computed at each computational time step. Let A be the matrix whose elements are the influence coefficients, a_{ij} . Let b_{ij} be an element of the matrix obtained from the inversion of A . Then the vortex loop strengths may be computed through the following system of equations,

$$\Gamma_i = - \sum_{j=1}^N b_{ij} \left(\vec{V}_\infty + \vec{w} \right)_j, \quad \text{for } i = 1, \dots, N. \quad (2.2)$$

The fuselage is assumed to be rigid which implies a time-independent matrix of influence coefficients, therefore allowing its inversion to be computed prior to the simulation and thus significantly enhancing computational efficiency.

For a lifting body, in addition to the N equations given by (2.2) applied to all the panels, another condition must also be satisfied in order to fix the precise value of the circulation around the body. This is the Kutta condition, which is satisfied along the entire trailing edge of the tailplane, thus accounting for the existence of lift.

Table 2.2: Fuselage geometric properties

Fuselage length	$2.04R$
Fuselage maximum width ¹	0.1891ℓ
Tailplane span	0.3201ℓ
Tailplane chord	0.0835ℓ
Tailplane airfoil section	NACA 0012
Shaft inclination angle	4° (forward)
Lower rotor hub x coordinate ²	0.3825ℓ
Lower rotor hub z coordinate ²	0.1930ℓ
Upper rotor hub z coordinate ²	0.2610ℓ
Propulsor hub x coordinate ²	1.0395ℓ
Propulsor hub z coordinate ²	0.0555ℓ

¹Excluding tailplane.

²Relative to fuselage nose.

The pressure on the fuselage surface may then be obtained from the unsteady Bernoulli equation,

$$\frac{p - p_\infty}{\frac{1}{2}\rho} = V_\infty^2 - |\vec{u}|^2 - 2\frac{\partial\phi}{\partial t} \quad (2.3)$$

where the unsteady potential $\partial\phi/\partial t$ is assumed to arise solely due to the variation of panel strengths with time and accounts for the disturbance to the velocity potential due to the convection of vortices within the main rotor wake. The velocity on the body surface is designated as \vec{u} and includes the contribution from all the vorticity in the computational domain as well as a near-field correction term that accounts for the self-influence of the vorticity on each panel by assuming it to be distributed as an equivalent vortex sheet.

In rotorcraft applications, a modified pressure coefficient is often used for convenience instead of the standard pressure coefficient, which is given by

$$C'_p = 100 \frac{p - p_\infty}{\frac{1}{2} \rho (\Omega R)^2}. \quad (2.4)$$

Note that the modified pressure coefficient is non-dimensionalised by rotor tip speed rather than the freestream velocity in order to avoid division by zero at hover, and is scaled by a factor of 100 purely for numerical convenience.

The helicopter model also features a simple horizontal tailplane rigidly attached to the fuselage body. It was designed to have a constant NACA 0012 airfoil section along its entire span. The tailplane is untwisted and its chord is parallel to the horizontal plane, $x - y$. It is modelled as a surface of discrete panels, each panel representing a closed vortex loop. Unlike the fuselage, the tailplane is allowed to produce lift and so the Kutta condition is also satisfied along its entire trailing edge, which means that the panel segments at the trailing edge of the tailplane are required to reproduce a vortex of vanishing strength.

2.4 Auxiliary Propulsor

The auxiliary propulsor consists of a five-bladed pusher propeller mounted at the tail of the helicopter such that its rotational axis is aligned with the longitudinal axis of the fuselage. A NACA 0012 airfoil section is used along the span of each blade, with no taper and with 30° of linear twist. The radius of the propulsor is 28% of the main rotor radius and its rotational speed is 4.25 times that of the main rotor.

The thrust generated by the propulsor can be controlled by altering its collective pitch. The blades and their attachments to the hub are assumed to be rigid, except for feathering motion. The hub of the propulsor is not modelled for further simplicity. The properties of the propulsor are summarised in table 2.1.

As with the main rotor blades, the computer modelling of the auxiliary propulsor blades follows the Weissinger L-method, introduced in section 2.7.

2.5 Vorticity Equation

The general laws of physics tell us that the motion of a fluid may be completely described by the conservation laws for the three basic properties: mass, momentum and energy. These laws are well established and can be formulated in many equivalent forms. Although the integral formulation of the equations is more generally valid, its direct applicability in control volume analysis is often limited. If more detailed information is required to investigate the fine, detailed behaviour of the fluid flow, the differential form of the conservation laws is normally the analytical technique employed. Also, approximations in the simplification of differential expressions can be made in order to not only ease their implementation in a modern computer, but also to save computational time when obtaining the solution. In particular, the Vortex Transport Model (VTM) is formulated in terms of a form of the momentum equation alone, known as the vorticity equation. The vorticity equation will be derived here, following the basic equations governing fluid flow in differential form.

The vorticity equation is then discretized and solved in a finite volume approach. The VTM uses a semi-Lagrangean adaptive grid composed of cells that can be dynamically created or destroyed in order to track regions of vorticity in the flow. In this manner, the regions in the flow where the vorticity field has zero magnitude are not contained in the computational domain. The equations governing fluid flow are taken as a starting point in deriving the vorticity equation. The mathematics and physics that underlie these equations are left to specialized books on the topic, for instance see [19]. Yet, there are some assumptions involved in those equations that should be pinpointed as they restrict the type of flow that can be modelled, namely the fluid is regarded as a *continuum* and is assumed to be homogeneous and Newtonian.

The equation of conservation of mass may be written in differential form as

$$\frac{\partial \rho}{\partial t} + \nabla \cdot (\rho \vec{V}) = 0. \quad (2.5)$$

The equation of linear momentum may be expressed as

$$\frac{\partial}{\partial t}(\rho \vec{V}) + \nabla \cdot (\rho \vec{V} \otimes \vec{V}) = -\nabla p + \nabla \cdot \bar{\tau} + \rho \vec{f}_e. \quad (2.6)$$

The equation of conservation of energy may be written as

$$\frac{\partial}{\partial t}(\rho e) + \nabla \cdot (\rho \vec{V} e) = \nabla \cdot (k \nabla T) - \nabla \cdot (p \vec{V}) + \nabla \cdot (\bar{\tau} \cdot \vec{V}) + \rho \vec{f}_e \cdot \vec{V} + q_H \quad (2.7)$$

where $\bar{\tau}$ is the viscous shear stress tensor, equal to

$$\bar{\tau} = \mu \left[\nabla \vec{V} + (\nabla \vec{V})^T \right] + \lambda (\nabla \cdot \vec{V}) \bar{I}. \quad (2.8)$$

In spite of the complexity and interdependence of the flow equations in this general case, it can be shown that for an incompressible flow with assumed constant fluid properties, equations (2.5) and (2.6) constitute an independent system for flow velocity and pressure. Furthermore, the equation of momentum can be written in many equivalent forms, one of them known as the vorticity equation, which is used in VTM formulation.

The derivation of the vorticity equation follows from the momentum equation. After expanding the derivatives in the left hand side of equation (2.6) and making use of equation (2.5) to drop out terms in \vec{V} , the non-conservative form of the momentum equation is obtained,

$$\rho \frac{d\vec{V}}{dt} = -\nabla p + \nabla \cdot \bar{\tau} + \rho \vec{f}_e. \quad (2.9)$$

Introducing the vorticity vector $\vec{\zeta}$,

$$\vec{\zeta} = \nabla \times \vec{V} \quad (2.10)$$

and using the vector identity,

$$(\vec{V} \cdot \nabla) \vec{V} = \nabla \left(\frac{V^2}{2} \right) - \vec{V} \times (\nabla \times \vec{V}) \quad (2.11)$$

in the inertia term $d\vec{V}/dt$, equation (2.9) becomes

$$\frac{\partial \vec{V}}{\partial t} - \vec{V} \times \vec{\zeta} = -\frac{1}{\rho} \nabla p - \nabla \left(\frac{V^2}{2} \right) + \frac{1}{\rho} \nabla \cdot \bar{\tau} + \vec{f}_e. \quad (2.12)$$

Taking the curl of the last equation, and after some algebra, the *Helmholtz* vorticity equation is obtained,

$$\frac{\partial \vec{\zeta}}{\partial t} + (\vec{V} \cdot \nabla) \vec{\zeta} = (\vec{\zeta} \cdot \nabla) \vec{V} - \vec{\zeta} (\nabla \cdot \vec{V}) + \frac{1}{\rho^2} \nabla \rho \times \nabla p + \nabla \times \left(\frac{1}{\rho} \nabla \cdot \bar{\tau} \right) + \nabla \times \vec{f}_e. \quad (2.13)$$

This equation can be significantly simplified if the flow is assumed to be incompressible and barotropic. By definition, a fluid is incompressible when the expansion rate of any fluid element is zero,

$$\nabla \cdot \vec{V} = 0. \quad (2.14)$$

This flow restriction results in the second term on the left hand side of equation (2.13) to vanish. This term accounts for the stretching of vorticity due to the contraction or expansion of fluid particles, which cannot take place in an incompressible fluid.

The barotropic flow assumption can be defined as the density of each fluid element to be dependent on its pressure only, $\rho = \rho(p)$. This approximation leads to the vanishing of the baroclinic term which is the third term in the left hand side of equation (2.13).

The resulting expression yields the unsteady vorticity equation

$$\frac{\partial \vec{\zeta}}{\partial t} + (\vec{V} \cdot \nabla) \vec{\zeta} = (\vec{\zeta} \cdot \nabla) \vec{V} + \nabla \times \left(\frac{1}{\rho} \nabla \cdot \vec{\tau} \right) + \nabla \times \vec{f}_e. \quad (2.15)$$

The viscous term can be further simplified if the kinematic viscosity coefficient is assumed to be constant, in which case it reduces to the laplacian of the vorticity,

$$\nabla \times \left(\frac{1}{\rho} \nabla \cdot \vec{\tau} \right) = \nu \nabla^2 \vec{\zeta}. \quad (2.16)$$

In helicopter flows, the free stream Reynolds number is typically at least 10^5 and thus viscosity effects become important only in a thin layer of fluid adjacent to the surfaces of the aerodynamic body or in very small scales, compared to the wake structure dimensions, where diffusion of vorticity becomes predominant, giving rise to the viscous decay of the small scale vortex structures of the helicopter wake.

In the Vorticity Transport Model the entire flow surrounding the helicopter is assumed to be inviscid, and the vorticity generated by the rotor blades, which is associated with the generation of aerodynamic loads there, is modelled as a local source of vorticity, \vec{S} . If no other sources of vorticity are considered, the last term in equation (2.15) is equal to the source term S . Equation (2.15) is then written as

$$\frac{\partial \vec{\zeta}}{\partial t} + (\vec{V} \cdot \nabla) \vec{\zeta} = (\vec{\zeta} \cdot \nabla) \vec{V} + \vec{S}. \quad (2.17)$$

In accordance with this equation, vorticity is first generated locally by numerically defined surfaces immersed within the fluid and is evolved through a three-dimensional computational domain under the action of the local velocity field. Hence, the problem can be conceptually divided in two parts. The first part is the model of the evolution of the rotor wake in a computational grid as described by equation (2.17) and the second part is the model of the blade aerodynamics that provides the vorticity source to be interpolated into the aforementioned computational grid.

2.6 Velocity Field

The velocity field can be calculated once the vorticity field is known. Taking the curl of the vorticity, such that

$$\nabla \times \vec{\zeta} = \nabla \times (\nabla \times \vec{V}) \quad (2.18)$$

which results in

$$\nabla \times \vec{\zeta} = \nabla(\nabla \cdot \vec{V}) - \nabla^2 \vec{V} \quad (2.19)$$

which, after the incompressible assumption, can be rewritten as

$$\nabla^2 \vec{V} = -\nabla \times \vec{\zeta} \quad (2.20)$$

which is a vector Poisson equation. The solution of this equation in an unbounded domain, that is, over the whole three-dimensional space, can be written as

$$\vec{V}(\vec{x}) = -\frac{1}{4\pi} \int_{\mathbb{R}^3} \frac{(\vec{x} - \vec{y}) \times \vec{\zeta}(\vec{y})}{|\vec{x} - \vec{y}|^3} d\mathcal{V}_{(\vec{y})} \quad (2.21)$$

which is the Biot-Savart equation.

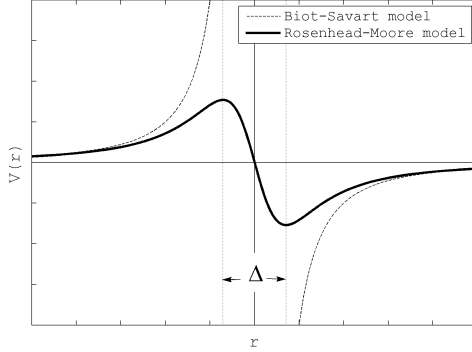


Figure 2.2: Comparison between the velocity field induced by the Biot-Savart kernel and by the Rosenhead-Moore kernel.

Equation (2.20) can be solved directly in differential form, but the complexity of the vortical structures in the rotor wake pose a serious difficulty in the derivation of boundary conditions. Instead, VTM solves a modified version of equation (2.21) that was proposed by Rosenhead, [20], who suggested the following approximation to the Biot-Savart equation,

$$\vec{V}(\vec{x}) = -\frac{1}{4\pi} \int_{\mathbb{R}^3} \frac{(\vec{x} - \vec{y}) \times \vec{\zeta}(\vec{y})}{(|\vec{x} - \vec{y}|^2 + \delta^2)^{3/2}} d\mathcal{V}_{(\vec{y})} \quad (2.22)$$

for some positive δ . This modification accounts for the finite core effects and was first used in the numerical calculation of aircraft trailing vortices by Moore, [21]. It is well suited for numerical implementation because the singularity is removed, thus allowing for a uniform distribution of vorticity in each computational cell.

In the VTM, the parameter δ is chosen such that the location of the maximum velocity induced by the vorticity in a cell coincides with the edge of that cell. Figure 2.2 shows the velocity induced by a vortex element in a plane orthogonal to the swirl axis, obtained using both equations (2.21) and (2.22). The boundaries of a computational cell of width Δ are also shown.

2.7 Blade Aerodynamic Model

The VTM calculates the blade aerodynamics through the Weissinger L-method [22], which is a modified version of the Prandtl lifting-line model that is also applicable to swept-back wings. This feature provides additional flexibility for rotorcraft applications since it allows the representation of blades with complex planform geometry.

A brief description of the salient aspects of the blade aerodynamic model is given next. For a more detailed explanation of the various features comprising this model see [23, 15, 24, 25].

The blade is divided into a finite number of discrete panels along the span of the blade. Each panel consists of a horseshoe vortex with the bound vortex positioned at the $1/4$ -chord. For each time step the blade rotates within the flow and a new row of spanwise panels consisting of trailed and shed vorticity is created in a fixed position relative to the trailing edge of the blade. This process is repeated at each time step, thus generating a vortex lattice that is allowed to convect by the local flow velocity.

At each time step the local flow velocity, \vec{V}_b , is calculated for each blade panel at a collocation point positioned at the $3/4$ -chord. The computed velocity is the vector sum of the free-stream velocity, the velocity induced by the vortex lattice within the blade aerodynamic model, the velocity induced by the remainder of the rotor wake and the velocity induced by blade structural motions, if any. Then the no-flow penetration condition is imposed at each collocation point, which forces the velocity component normal to the blade at those points to be zero. This results in a set of simultaneous equations that can be solved for the bound vorticity over the blade, $\vec{\zeta}_b$, and the strength of the trailed and shed vorticity produced over that time step. This, in turn, can be expressed as

the source term of equation (2.15),

$$\vec{S} = -\frac{d\vec{\zeta}_b}{dt} + \vec{V}_b \nabla \cdot \vec{\zeta}_b \quad (2.23)$$

where the first term on the left hand side represents the shed vorticity and the second term the trailed vorticity.

Although the blade aerodynamic model is coupled with the wake evolution model through the source term, \vec{S} , they can be regarded as two distinct parts of the overall VTM, as mentioned earlier. Each of these parts can be solved with a different time step, allowing the problem of having two different timescales to be resolved. One time scale is associated with the lower frequency of the evolution of the wake, and the other can be attributable to the high frequency unsteady blade aerodynamics and rotor-blade dynamics. In practice, this can be accomplished through a global time step Δt for solving the wake evolution within the computational domain and a lower time step, or substep $\Delta t/m$, to solve the evolution of the blade vortex lattice, within the blade aerodynamic model. If the blade sweeps by an angle $\Delta\psi$ during the global time step Δt , then for each substep it would sweep an angle $\Delta\psi/m$. At each substep the system of horseshoe vortices is allowed to grow as described previously and the vorticity generated is calculated. After m substeps the total vorticity source is obtained as the sum of the intermediate vorticity generated at each substep and it is introduced in the computational domain of the wake through interpolation of the vortex lattice.

The Weissinger L-method is based upon potential flow theory and so it does not take into account the effects of Reynolds number and Mach number that are experienced by real airfoil sections in a broad range of helicopter flight conditions. In order to include this effects in the model, tables containing the lift coefficient, $C_L(\alpha, Re, M)$, are given as an input to the VTM. These tables can be obtained either numerically from an external solver or directly from experimental data, if available. The full angle of attack range of $[0^\circ, 360^\circ]$ is given since the blade can experience reverse flow. If the lift coefficient data was obtained through an incompressible model, it is modified with the application of the Prandtl compressibility correction. Coefficients of drag and moment about the 1/4-chord are also included in the tables.

At the beginning of each time step, the lift coefficient is obtained from the respective table according to the flow conditions at each airfoil section and is used to modify the no-flow penetration boundary condition at the correspondent collocation point. The strength of the bound vorticity is then calculated, as described previously, and so a different result is obtained. In this manner, the model is able to capture the behaviour of the airfoil in its stall regime.

The VTM also incorporates a simple dynamic stall model that can track the main features of the dynamic stall effects in the blade loading. However, as already mentioned in Section 2.1, certain three-dimensional effects cannot be captured by the blade aerodynamic model, since the airfoil data included in the model is two-dimensional. One of these effects, mentioned by Line, [25], is the stall-delay that is known to be a result of the influence of the blade rotation in the boundary-layer profile of the two-dimensional airfoil sections.

2.8 Trim Model

The present study focuses on the aerodynamic interactions that take place at a single flight condition, in which the helicopter model described earlier is required to flight in a horizontal rectilinear path, with no sideslip, at constant forward speed with an advance ratio of $\mu = 0.15$. At this advance ratio the aerodynamic interactions between the various helicopter components have been predicted to be more diverse and more interesting of being investigated, [2]. In order to maintain this particular flight condition the resultant forces acting on the rotorcraft should balance each other such that their vector sum is zero, as a consequence of Newton's second law. In particular, it implies that the lift generated by the rotorcraft should balance its own weight, the drag should balance the propulsive force generated by the main rotor plus auxiliary propulsor and the resultant side force should vanish. Conditions on the resultant moments acting on the rotorcraft should also be satisfied in order to ensure the rotorcraft has a fixed overall orientation along its flight path. Hence, it is required that the resultant moment acting on the rotorcraft vanishes. Moment equilibrium may be calculated with respect to an arbitrary reference point, which, for convenience, is chosen to be the centre of the lower rotor hub.

It is important to distinguish between instantaneous and average forces acting on the helicopter. On the one hand, the instantaneous forces change with time in both magnitude and direction. Consider, for instance, a blade from one of the rotors. That blade is subjected to an aerodynamic loading that will change with time because it depends on the relative velocity field, which in turn will vary while the blade is rotating. Average forces, on the other hand, are defined by the average of the instantaneous forces over n rotor revolutions. The same definitions also apply to the moments acting on the system.

The purpose of the trim model is thus to find the control inputs to the main rotor and tail propulsor that drive the helicopter into an equilibrium condition. However, the time varying aerodynamic loads acting on the helicopter lead to a dynamic trim process that continuously adjusts the control inputs during the simulation in order to approach equilibrium. This process can be summoned in

the form of a first order dynamic system,

$$\frac{d\vec{\theta}}{dt} = \vec{f}(\vec{\theta}) \quad (2.24)$$

where $\vec{\theta}$ is the vector of pitch inputs given by

$$\vec{\theta} = [\theta_0^u, \theta_{1s}^u, \theta_{1c}^u, \theta_0^\ell, \theta_{1s}^\ell, \theta_{1c}^\ell, \theta_0^p]^T \quad (2.25)$$

and \vec{f} is a vector valued function that gives a linear relationship between the rate of change of the control inputs and the instantaneous resultant forces and moments acting on the system,

$$\vec{f} = K (\vec{C}_F^* - \vec{C}_F) . \quad (2.26)$$

The matrix K is a 7×6 coupling matrix and is introduced in [2], although not taking into account the propulsor control input. The vector \vec{C}_F^* contains the prescribed target load coefficients on the vehicle, given by

$$\vec{C}_F^* = [-C_D, 0, C_W, 0, 0, 0]^T \quad (2.27)$$

and \vec{C}_F represents the vector of overall aerodynamic force and moment coefficients that are produced by the rotors and other lifting components, and may be written as

$$\vec{C}_F = [C_{F_x}, C_{F_y}, C_{F_z}, C_{M_x}, C_{M_y}, C_{M_z}]^T . \quad (2.28)$$

The components of \vec{C}_F are written with respect to a global Cartesian reference frame with origin at the lower rotor hub centre and axes aligned as shown in figure 2.1. Each component is regarded as positive in the corresponding positive axis direction.

After the initial conditions have been set, the system would evolve through a transient phase until the aerodynamic environment and loads eventually reach a steady state. Static equilibrium may then be pursued if the equilibrium equations are formulated in terms of the long-term average of forces and moments. Hence, the system is considered to be trimmed when

$$\vec{C}_F^* - \vec{C}_F^{av} = 0 \quad (2.29)$$

where \vec{C}_F^{av} designates the long-term average of \vec{C}_F . Note that this simplification is only valid if the amplitude of the instantaneous quantities remains within acceptable bounds.

The following methods and simplifying assumptions were incorporated into

the trim algorithm:

- The matrix K is defined such that the response of the collective and cyclic controls to the forces and moments produced by the main rotor system is decoupled.
- The collective pitch inputs of both upper and lower rotors are varied simultaneously in order to modify the thrust produced by the main rotor, whereas they are varied differentially to trim the net yawing moment of the system. Hence, instead of adjusting directly the collective pitch of the upper and lower rotors, the idea is to control a single collective pitch angle and a differential collective angle defined by $\bar{\theta}_0 = (\theta_0^u + \theta_0^\ell) / 2$ and $\Delta\theta_0 = (\theta_0^u - \theta_0^\ell) / 2$, respectively.
- The equilibrium of the system in terms of pitch and roll is achieved by varying the cyclic pitch inputs. The same cyclic pitch inputs are applied to both upper and lower rotors.
- The weight coefficient is denoted by C_W and accounts for the total weight of the vehicle. In the present analysis, the weight coefficient is fixed at $C_W = 0.012$. Following [26], an equivalent flat-plate parasite-drag area of $1/25^{th}$ of the main rotor disc area is used in order to calculate the drag of the system at $\mu = 0.15$, which yields $C_D = 0.00072$. The values assumed for the weight and drag coefficients of the system are similar to those of the XH-59A helicopter, [27].
- The main rotor contributes partially to the forward component of thrust that is required to maintain the forward speed of the helicopter. Since the blades are very rigid and no flap hinges are used, the longitudinal tilt of the main rotor cannot be achieved through cyclic pitch controls to tilt the tip path plane relative to the rotor shaft. Instead, the high control power of the main rotor allows very direct control of the rotor shaft tilt relative to the flight path. It is considered that the pitching moment produced by the main rotor is enough to cause its tip path plane and rotor mast to incline 4° forward, thus allowing the main rotor to contribute to the forward component of thrust.
- The longitudinal force balance is ensured by the propulsive force generated by the tail propulsor, which may be adjusted through the variation of its own collective pitch.
- The resultant lateral force can be assumed negligible and therefore is not trimmed in the present calculations.

3 VALIDATION OF THE VTM COMPUTER PROGRAMME

The helicopter model described previously does not accurately mimic any particular helicopter prototype but can only, at best, be representative of full-scale helicopter models such as the Sikorsky X2 and the XH-59A. Therefore, no direct comparison between the documented experimental data of those prototypes and the computational results of the present model has been attempted due to the obvious differences in the main rotor, fuselage geometry and auxiliary propulsive device. However, helicopter models from several widely-used experimental sets of data have been recreated and incorporated into the VTM for validation purposes. This chapter gives a brief qualitative description of the VTM predictions against several experiments for different flight conditions.

The results of a validation of the VTM in hover flight are reported in [15], where it is compared against the well-known experimental data from the work of Caradonna and Tung [28]. The experimental model comprised an isolated two-bladed rotor with 7.5 ft (2.286 m) diameter and 0.5° of precone angle which was cantilever-mounted at the drive shaft. The blades were untwisted and un-tapered with an aspect ratio of 6 and featured a NACA 0012 airfoil section along the whole span. Blade collective pitch could be manually adjusted. Test cases for three collective pitch settings and several rotational speeds were conducted with pressure data being collected from 60 pressure tubes along each blade. Wake data was also acquired through a hot-wire probe mounted beneath the rotor. Data from the wire was measured at several points along the tip vortex trajectories and allowed to assess both the tip vortex geometry and strength. The corresponding computational rotor model was compared against the experimental one in terms of blade loading with the rotor operating at 150 m/s tip speed and generating a constant thrust coefficient of 0.0079. The results, presented in [15], revealed the VTM to agree well with the relatively sparse experimental data, with a maximum relative difference of about 8% close to the blade tip. The location of the tip vortices in the flow downstream of the rotor was also subject of comparison, under the same rotor operating conditions. The tip vortex positioning was measured in terms of radius and vertical displacement beneath the rotor versus vortex age. The VTM results were consistent with the experimental data, particularly over the first 270° of vortex age,

beyond which the computational data became increasingly scattered due to the far wake unsteadiness. Furthermore, results showed a slight overprediction of the axial contraction rate of the tip vortices. The VTM was also compared against Kocurek and Tangler's widely-used empirical wake trajectory, [29], this time showing the opposite trend – an underprediction of the tip vortex axial contraction.

The VTM has been validated in steady forward flight against the experimental data produced by Harris, [30]. This data was obtained from wind-tunnel tests to an isolated four-bladed articulated rotor model over a range of flight speeds. The rotor was trimmed to generate a prescribed thrust coefficient, with the cyclic pitch controls held fixed, and the flapping behaviour of the rotor disk was measured. Two sets of results corresponding to different computational versions of the VTM were compared against the experimental data from Harris and are presented in [31] and [15]. The two computational versions differed from each other in the number of cells used to resolve the rotor wake and in the number of grid levels that formed the nested grid structure. The numerical results obtained using these two different versions were compared against Harris measurements of longitudinal and lateral tilt of the rotor disc as a function of advance ratio. The predicted values obtained by both versions of the VTM showed good agreement with the experimental data. The computed curves for the lateral disc tilt were enclosed within the experimental error bounds for all advance ratios tested, whereas the longitudinal curves revealed a slight overprediction for advance ratios beyond 0.15 that was attributed to a deficiency in the blade aerodynamic model at high advance ratio.

A more relevant account of the validation of the VTM, regarding the rotor configuration employed in the present study, is that given by references [1] and [2] whereby a coaxial rotor system is analysed. Results from the wind-tunnel tests reported by Harrington, [32], and Dingeldein, [26], constituted the sources of the experimental data against which the VTM results were compared. Harrington conducted an investigation on the performance of coaxial and single rotors in hover and under static-thrust conditions. Two different coaxial rotors were tested but only one of them, referred to as 'rotor 1' in Harrington's paper, was compared against the VTM simulations. Dingeldein also adopted this particular rotor system in his study of coaxial rotor performance in both hover and level flight. The rotor system consisted of two rotors arranged in a coaxial configuration, each featuring two blades attached to a simple hub allowing for feathering motion. The hubs were assembled into their respective drive shafts through a single horizontal pin thus forming a teetering design. The blades were untwisted, combined linear taper in plan form with non-linear spanwise thickness distribution and were composed of NACA four-digit symmetrical air-

foil sections. The rotor system yielded a rather low solidity of 0.054, relative to the value of 0.127 that is characteristic of the rotor system considered in the current work, but still constitutes a reliable model for comparison with VTM predictions. The general properties of Harrington's coaxial rotor are gathered in table 3.1.

Table 3.1: Properties of Harrington's rotor 1

Rotor Radius	12.5 ft (3.81 m)
Number of rotors	2 (coaxial arrangement)
Blades per rotor	2
Interrotor spacing	19% of rotor radius
Root cut-out	13% of rotor radius
Rotor solidity ¹	0.054

¹Based on the projected area.

Reference [1] shows a comparison between the predictions of the VTM and the experimental results of Harrington in terms of nondimensional rotor power versus thrust for the hover case. Both the experimental and computational models used differential collective pitch in order to trim the yawing moments produced by the coaxial rotor. The VTM implemented two different drag models in its simulations. For low values of thrust coefficient, the power predicted by both models was very close to the experimental data and started to depart gradually beyond a thrust coefficient of 0.003, although falling within the experimental error margin. The observed differences were attributed to the profile drag models employed.

The steady level flight case was also considered in Ref. [1], where the VTM predictions were compared against Dingeldein's data. The coaxial rotor was trimmed in yaw and its thrust coefficient and tip speed were held constant throughout the experiment and equal to 0.0048 and 469 ft/s (143 m/s) respectively. An equivalent single rotor with the same solidity as the coaxial rotor was also modelled in this study. It consisted in a conventional, articulated rotor composed of four blades having the same properties as the blades of the coaxial rotor. Figure 3.1 shows the results of a comparison between the VTM results, with respect to the coaxial and equivalent single rotors, and Dingeldein's measurements for the variation of power consumption with advance ratio. The results obtained with the VTM revealed a systematic underprediction but followed the shape of the experimental data points very closely. As in the hover case, the observed differences were ascribable to deficiencies in the profile drag model of the rotor blades.

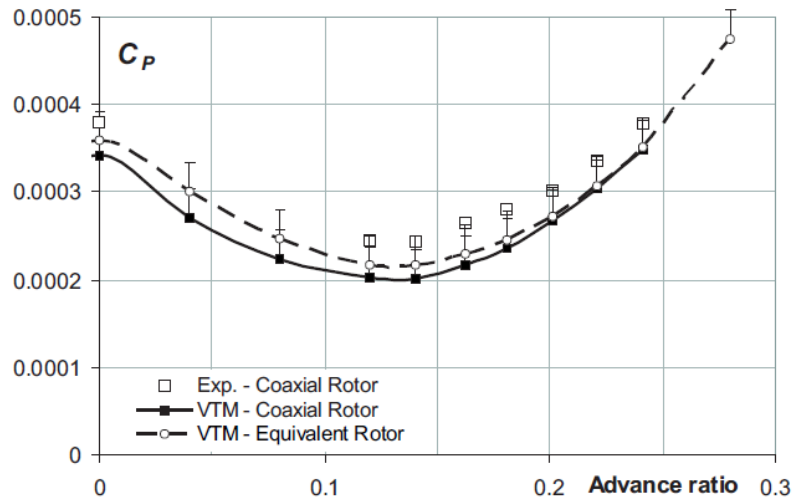


Figure 3.1: Comparison of the overall power consumption with advance ratio in forward flight between the VTM simulations and Dingeldein's experimental data. (Adapted from Ref. [1].)

The same rotor configuration was replicated in Ref. [2] and was used in VTM simulations. However, a systematic correction was applied to the numerical results since the previous drag model used in the VTM simulations was based on the original results of Harrington for the hover case despite the small offset between Dingeldein's and Harrington's measurements of power required by the rotor to hover. Figure 3.2 compares the VTM predictions of the variation of total power with advance ratio obtained from two distinct simulation cases against the experimental data of Dingeldein. The data sets yielded by these distinct cases were named VTM-dynamic and VTM-static data. The former corresponds to a single simulation where the coaxial rotor was accelerated from hover to $\mu = 0.35$, while the later corresponds to a simulation where the advance ratio was held fixed for each of the advance ratios of interest. This duality of methodology arises as part of an assessment of the ratio between computational efficiency and accuracy. Also plotted in this figure is the curve labeled 'VTM-dynamic (filtered)' that was obtained from the dynamic data by removing all fluctuations at greater than blade-passing frequency.

This time, computational predictions for the total power consumption revealed a better agreement with Dingeldein's experimental data, with the static case yielding a slight underprediction of power consumption in hover and at advance ratios between 0.10 and 0.20, and a small overprediction beyond. The filtered dynamic case also revealed slighter underprediction for all the advance

ratios of the experimental data. However, it predicted a significantly higher power consumption than the static case for advance ratios in the pre-transitional regime ($\mu < 0.10$).

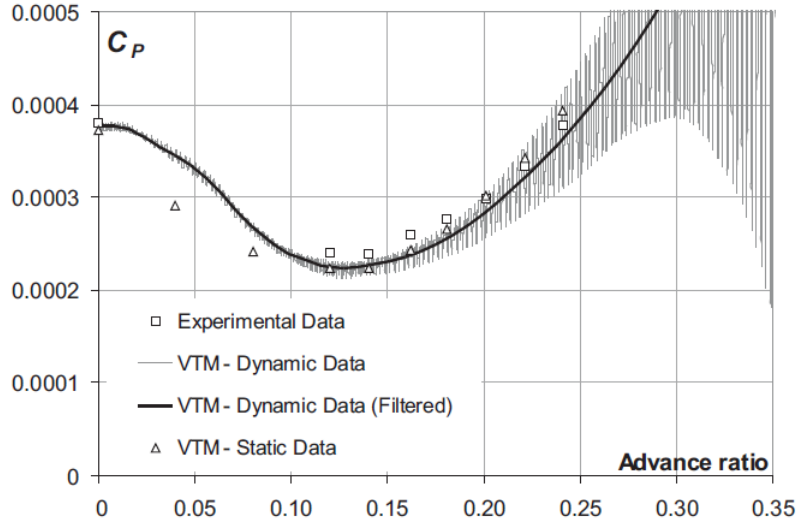


Figure 3.2: Comparison of the overall power consumption with advance ratio in forward flight between the VTM simulations and Dingeldein's experimental data using the corrected drag model. (Adapted from Ref. [2].)

Other successful validations of the VTM include rotor-fuselage interactions, in which the VTM was used to predict the pressure distribution over the isolated ROtor Body INteraction (ROBIN) fuselage at forward flight and over a number of advance ratios including $\mu = 0.15$. The analytic definition of the ROBIN body is given as an appendix to the work of Mineck and Gorton, Ref. [33], together with tabular listings of measured unsteady pressure data. Kenyon and Brown, Ref. [34], conducted the VTM simulations and compared its predictions to the measurements of Freeman and Mineck, [35]. Although it is reported that the quality of the predictions decreased at some locations towards the tail of the fuselage, the VTM results were generally in very close agreement with the experimental data.

The VTM was also coupled with a particle dynamics model for simulation of the brownout effect, where the helicopter model is operating close to the ground in desert or dusty conditions, and was successfully validated against both empirical correlations and flight test data, Ref. [36].

4 RESULTS

The helicopter rotor wake is dominated by strong vortices that are trailed from the tips and roots of each rotor blade. Since the helicopter is flying forward at an advance ratio $\mu = 0.15$, these vortices are convected behind as well as below the rotor. The fundamental process of the formation of the blade wake and tip vortices is similar to that of a fixed wing. However, in a system of rotating wings the wake and tip vortices produced by each blade can remain close to the plane of rotation and can have strong induced effects on the velocity field there, which in turn can change the lift distribution at the blades and constitute a source of unsteadiness. Although the VTM models the blade wake as a vortex lattice of trailed and shed vorticity, as mentioned in section 2.7, at this forward flight speed the effects of the trailed vortices, and specially those of the tip vortices, on modifying the velocity field at the plane of the rotor are generally more important than the effects of the shed vortices, Ref. [37]. The intricate process of tip vortex formation will not be discussed here but a comprehensive account on this topic is given by Ref. [38], while the evolution of general vortex filaments in three-dimensional ideal flows is treated in Ref. [39] and under a more mathematical standpoint in Ref. [40]. In a contrarotating coaxial rotor arrangement, however, the bound vortex to each blade as well as the shed vorticity immediately behind each blade can gain significant importance, as the blades pass close to each other as they rotate.

This section provides an account of the several aerodynamic interactions that are induced by the main rotor wake on the main rotor itself and on the other components of the helicopter model. It also gives a description of the individual contributions of each component in modifying the main rotor and propulsor wakes and hence the velocity field around the helicopter and its effects on rotor loads and overall performance.

4.1 Wake Structure

Consider the simple case first, where only the main rotor is present. Two kinds of aerodynamic interactions are possible, namely the interaction between the main rotor and the vortex filaments and the mutual interaction between the individual vortex filaments. If none of these interactions is modelled, then the wake geometry can be described by a Prescribed Wake Model with rigid wake

(Ref. [4]) and the result, at a given time t , is shown in figure 4.1. Only the tip vortices produced by two of the blades are shown for clarity. Different colours were used to distinguish the filament produced by the upper rotor from that produced by the lower rotor. The geometry obtained consists of a pair of skewed, undistorted helices symmetric with each other with respect to the $x - z$ plane.

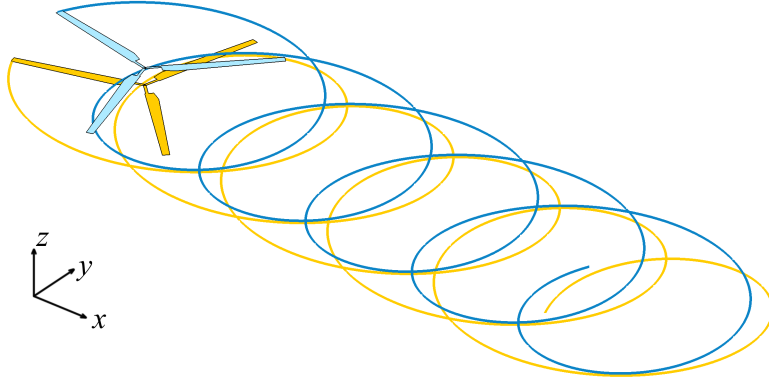


Figure 4.1: Three-dimensional view of the tip vortex filaments trailed by two blades of the coaxial rotor system as given by the prescribed wake model.

Figure 4.2 shows the main rotor and the complex set of all tip vortex geometries produced by all the blades when the observer is located over the main rotor. It is apparent from this view that each vortex filament describes a prolate cycloid. It can be seen that the vortices cross the blades at different orientations although physical intersection only occurs in the lower rotor since the tip vortices produced by the upper rotor are convected underneath it.

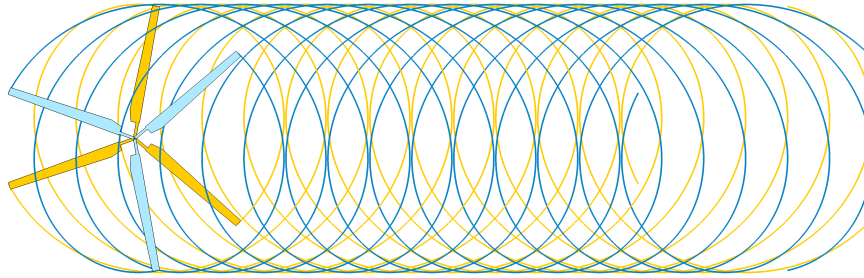


Figure 4.2: Tip vortex filaments trailed by the coaxial rotor system as viewed from above.

Now consider the case where interactions are modelled. Figure 4.3 shows the main rotor and the set of tip vortex tubes produced by its rotor blades in four different perspectives. The surface that bounds these vortex tubes was

obtained directly from the vorticity field around the rotor and consists in the set of all points where the magnitude of the vorticity is constant. As before, distinct colours are associated with the iso-surfaces of vorticity generated by each of the main rotors. A bottom view of the configuration is also provided in appendix, figure A.3.

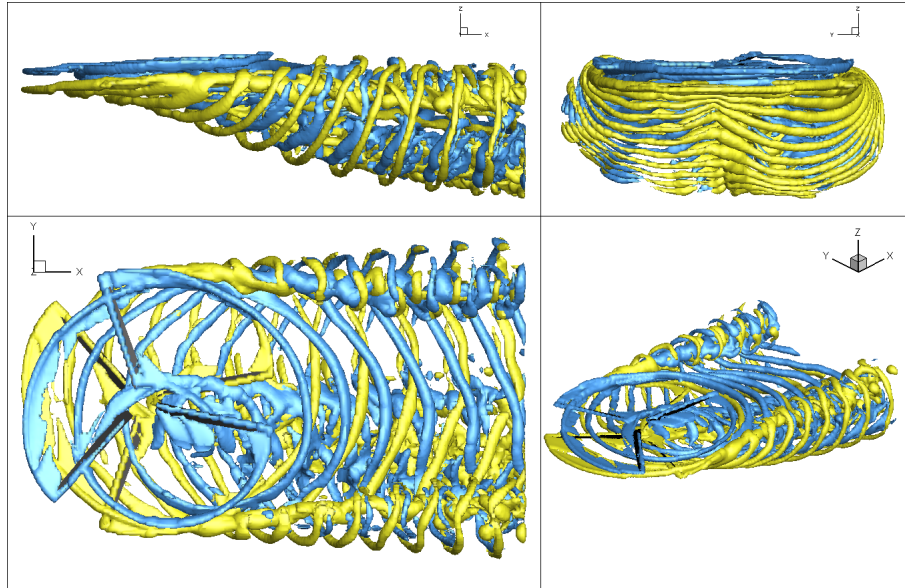


Figure 4.3: Iso-surfaces of vorticity magnitude generated by the main rotor operating in isolation at advance ratio $\mu = 0.15$. (Iso-surfaces from different rotors rendered separately in distinct colours.)

Comparison between figures 4.1 and 4.3 reveals a significant change in the idealized helicoidal wake structure. Now the vortex tubes are allowed to interact with each other which results in the distortion of the wake. It is evident that along the lateral edges of the wake and starting shortly behind the main rotor the tip vortices tend to roll-up into a pair of concentrated, counter-rotating “super-vortices”. The symmetry in the $x - z$ plane is also destroyed due to the mutual interaction between the vortices inside the rotor wake. Another feature that departs from the idealized model of figure 4.1 is that the vortices generated at the leading edge of the disk are initially convected along the rotor disk plane whereas the vortices generated at the trailing edge of the rotor are readily convected away from that plane. This is a result of a small region of upwash velocity at the leading edge of both rotor disks and a strong longitudinal inflow gradient.

The wake geometry gains another degree of complexity if the tail rotor wake is also simulated. Figure 4.4 shows the iso-surfaces obtained from the vorticity

field around the main rotor and tail rotor.

It can be seen that the wake generated by the tail propulsor is strongly disturbed by the induced effects of the tip vortices. The tube-shaped geometry of the propulsor wake is disrupted due to the strong interaction with the root vortices of the main rotor. The main rotor wake is also influenced by the vorticity generated by the propulsor, especially downstream of the propulsor where the disruption of the tip vortices originated in the lower rotor blades is apparent. The mutual effects between the main rotor and tail rotor wakes can be classified as an “indirect” mode of interaction.

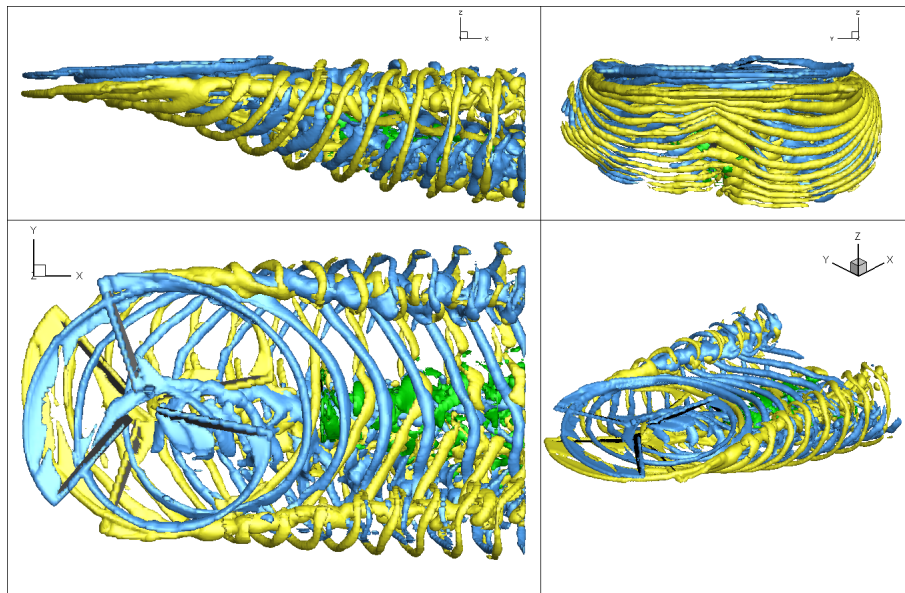


Figure 4.4: Iso-surfaces of vorticity magnitude generated by the main rotor and propulsor at advance ratio $\mu = 0.15$. (Iso-surfaces from different rotors rendered separately in distinct colours.)

Finally, consider the full helicopter configuration consisting of the main rotor, tail propulsor, fuselage and tailplane. Figure 4.5 shows four different views of the wakes generated by the lifting components of this configuration. Again, different colours were used to shade the different vortex structures generated by each component.

It is evident from the top view ($x - y$ plane) that the root vortex structures of the main rotor as well as the propulsor wake are skewed towards the port side of the configuration. This is due to the strong interaction between these vortex structures and the super-vortices. Indeed the skew of the root vortices produced by the main rotor is also present in the previous configurations, namely the isolated main rotor and main rotor with propulsor, as can be seen in the

top views of figures 4.3 and 4.4 respectively. It can be inferred that the super-vortex trailing down the port-side is stronger than the one at the starboard-side causing an asymmetry in the flow field and the skew of the root-vortex structures. The combined effects of the super-vortices and the root-vortices causes the propulsor wake to be skewed as well. However, the trailing vortex from the starboard tip of the tailplane is close enough to the starboard-side super-vortex to escape the influence of the port-side super-vortex and instead reveals a skew towards the starboard-side, which allows it to convect without any significant distortion. It is also visible the helicoidal geometry of the trailing vortices produced by the port-side of the tailplane that are the result of the interaction between these vortices and the root vortices from the main rotor.

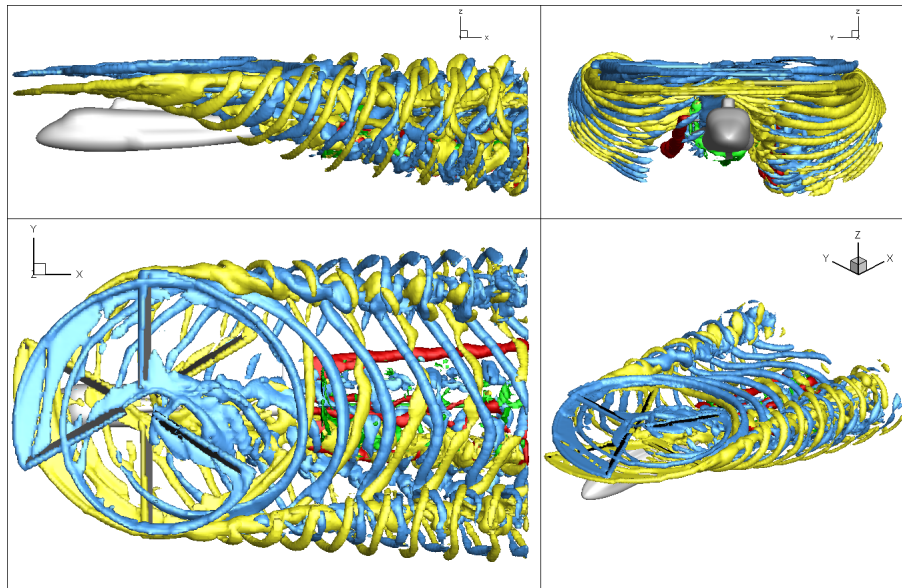


Figure 4.5: Iso-surfaces of vorticity magnitude of the full helicopter configuration at advance ratio $\mu = 0.15$. (Iso-surfaces from different components rendered separately in distinct colours.)

A comparison between the lateral views of figures 4.4 and 4.5 shows that there is a strong indirect interaction between the fuselage and the main rotor wake. It can be observed the upward displacement of the main rotor wake of the full configuration relative to the configuration were the fuselage is absent. The fuselage is responsible for altering the local velocity field, such that the front part of the lower rotor suffers a small upwash that will affect the angles of attack over that region, and hence the blade loading and rotor trim (Ref. [4]). The opposite behaviour occurs in the rear part of the lower rotor disk, where the fuselage causes a small downwash.

Figure 4.6 shows a direct mode of interaction between the tip vortices generated by the main rotor and the tailplane and propulsor. The impingement of tip vortices results in pressure fluctuations on the upper surface of the tailplane that integrate to produce a periodic loading that may cause high vibrations in the tailplane that may be transmitted to the fuselage. In order to maintain the aircraft in pitch equilibrium, the trim algorithm tries to compensate the down-load on the tailplane thus modifying significantly the loading distribution of the main rotor system.

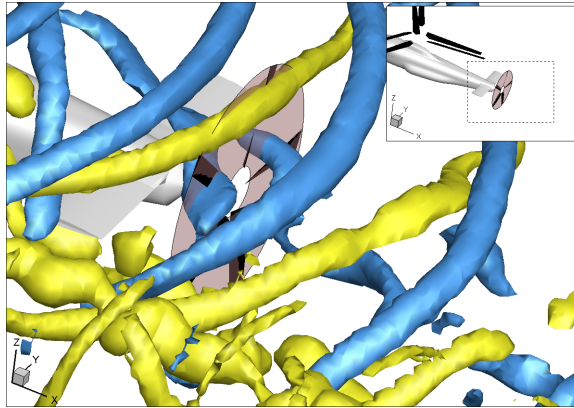


Figure 4.6: Iso-surfaces of vorticity magnitude showing the close-passage of the tip vortices from the main rotor on the upper surface of the tailplane and the ingestion of these vortices by the propulsor.

4.2 Isolated Coaxial Rotor

The sources of aerodynamic interaction involving the main rotor system will be exposed in this section. In order to better track these interactions the approach introduced in the previous section will be adopted here, in which configurations having a different degree of complexity are analysed and compared with each other.

When operating in isolation, the main rotor aerodynamic characteristics are influenced only by the mutual interactions between the main rotor and its wake. In order to have a better understanding of the aerodynamic environment experienced by the main rotor, figure 4.7 shows the distribution of inflow, $-v_i R^{-1} \Omega^{-1}$, along two representative blades, one on the upper and the other on the lower rotor, as a function of their azimuth. The same method is used to plot the distribution of blade loading over the blades of the main rotor in figure 4.9.

Figure 4.7 shows localized curved ridges that represent the close-passage of a tip vortex near the blade and are responsible for strong and localized radial

gradients of inflow velocity on both rotor disks. The tip vortices can interact with the rotor that has originated them or with a different rotor. For instance, the vortices originating in the upper rotor meet the blades of the lower rotor and the tip vortices originating from the leading edge of the upper and lower rotors interact with the upper and lower rotors respectively since they travel some distance along the rotor disk plane, as can be seen in figure 4.8.

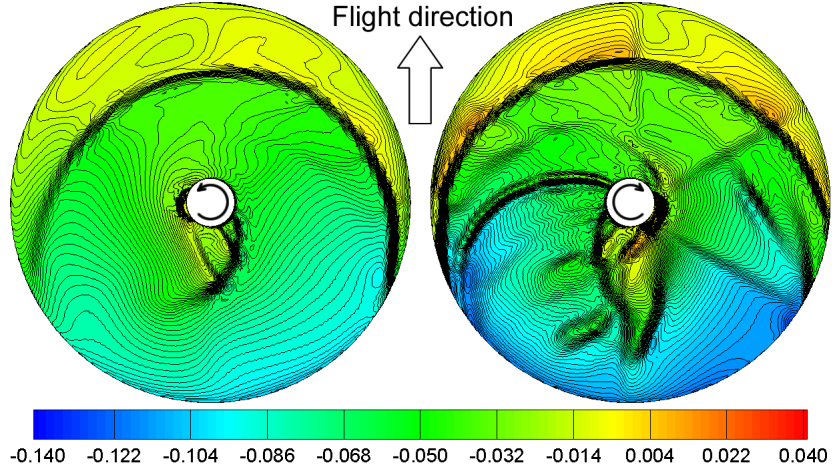


Figure 4.7: Distribution of inflow over the blades of the upper and lower rotors during a complete rotor revolution. Left: upper rotor. Right: lower rotor.

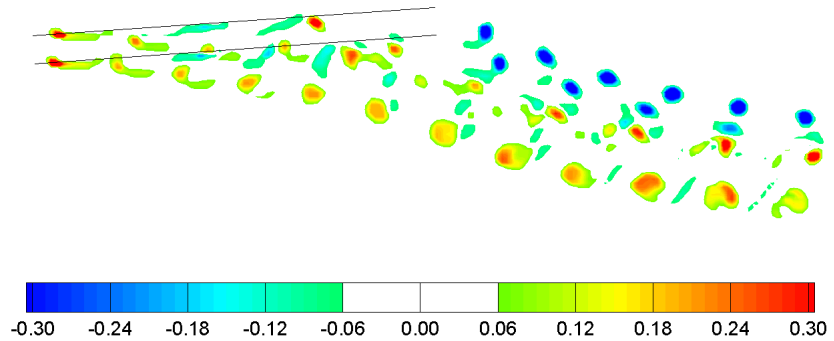


Figure 4.8: Contour plot of the y -component of non-dimensional vorticity (normalized by its maximum value ζ_{max}) in the $x - z$ plane for the isolated main rotor. Region of $|\zeta_y/\zeta_{max}| < 0.06$ not plotted for clarity.

The reason why these leading edge vortices are initially convected along the plane of the rotor is due to the very small inflow magnitude in the region between the leading edge of the disks and the first localized curved ridge. The small inflow is due to an upwash introduced by the system of previously generated tip vortices. It can be verified that the upper rotor wake disturbs the aerodynamic environment of the lower rotor more strongly than the lower rotor

on the upper, which is a consequence of the direct impingement of vortices from the upper rotor into the lower rotor.

It can be seen that the tip vortices interact with the rotor blades under different relative orientations. The interaction between a vortex and a rotor blade is called a Blade-Vortex Interaction (BVI) and can be classified into two different groups, according to two limiting conditions on the angle between the vortex axis and the blade. When the vortex axis and the blade are perpendicular to each other the interaction is called a Low Speed Interaction (LSI) and when they are parallel it is called an High Speed Interaction (HSI). The LSI is responsible for an increase in overall power consumption and low harmonic loading while the HSI is responsible for noise, vibration and higher harmonic loading, Ref. [41].

An HSI type of interaction can be observed in figure 4.7 as the straight radial ridges that are induced when the blades of the upper and lower rotors pass over each other. These ridges are clearly visible only on the lower rotor. The frequency of the blade over-passage type of interaction is 6 rev^{-1} . The same figure also shows a complex interaction at the rear of both rotor disks that results from the interaction between the rotors and the root-vortices. Again, the lower rotor is visibly more affected than the upper rotor.

Figure 4.9 shows a contour plot of the blade loading distribution experienced by a representative blade of both rotor disks and during one rotor revolution. The loading on the blade is higher in the region close to the tip and in the advancing side of both rotors, which is a consequence of the rigid rotor system that was employed in the simulations.

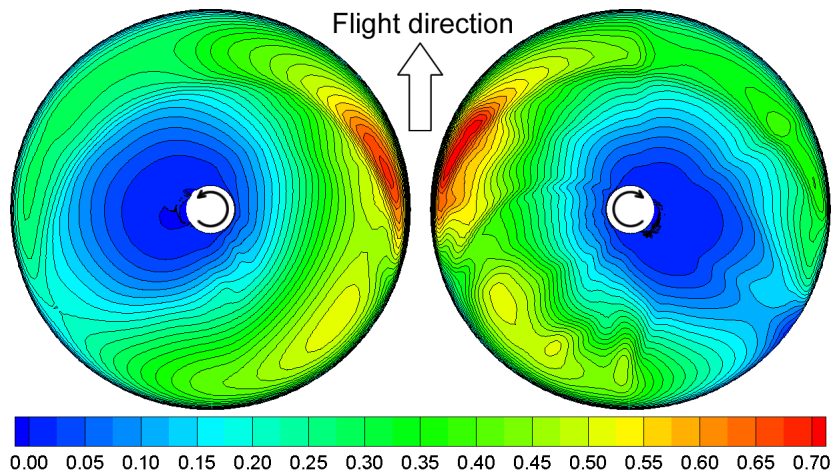


Figure 4.9: Distribution of loading over the blades of the upper and lower rotors during a complete rotor revolution. Left: upper rotor. Right: lower rotor.

Figure 4.9 shows that the concentration of loading on the upper rotor occurs at the right-hand side while on the lower rotor occurs on the left hand side, which is guaranteed by the trim algorithm in order to achieve rolling moment equilibrium.

The integrated blade loading over all the blades of a particular rotor yields the thrust produced by that rotor. Figure 4.10 shows the thrust coefficient as a function of azimuth over a complete rotor revolution as well as the respective frequency spectrum.

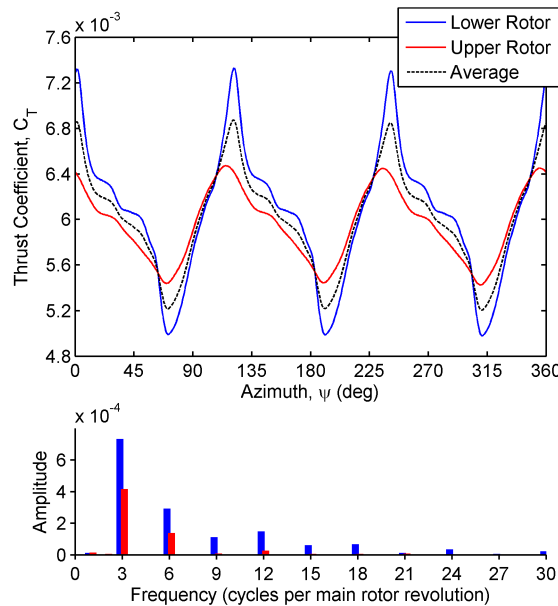


Figure 4.10: Thrust coefficient generated by the upper and lower rotors of the coaxial system as a function of azimuth and respective frequency spectrum.

The average thrust coefficient with respect to the upper and lower rotors is also included and represents half of the total thrust produced by the main rotor. The mean thrust over one revolution is similar between both rotors with the lower rotor producing a mean thrust coefficient that is 1.8% greater than that produced by the upper rotor (table A.1). However there is significant unsteadiness that is a direct consequence of the several aerodynamic interactions alluded to earlier.

Figure 4.10 shows the frequency spectrum of the thrust signal for the upper and lower rotors, that was obtained through a discrete Fourier transform of the signal. It shows that the frequencies occur as multiples of three, as a consequence of the simultaneous action of the three blades in producing tip and root vortices over each revolution. The higher amplitude of the signal occurs at 3 rev^{-1} , and can be attributable not only to the blade-vortex interaction

but to the aerodynamic properties of the rigid blades that constitute each rotor of the coaxial system. To see this, consider the case where no interactions occur between the rotors and their wakes. If a Uniform Inflow Model (UIM) is used to obtain the thrust produced by each of the rotors it can be verified that the 3 rev^{-1} component still appears in the thrust coefficient as a function of azimuth. Figure 4.11 shows the particular case where only the upper rotor is considered in the analysis and compares the thrust function obtained using the VTM and the uniform inflow model, at the same average thrust coefficient.

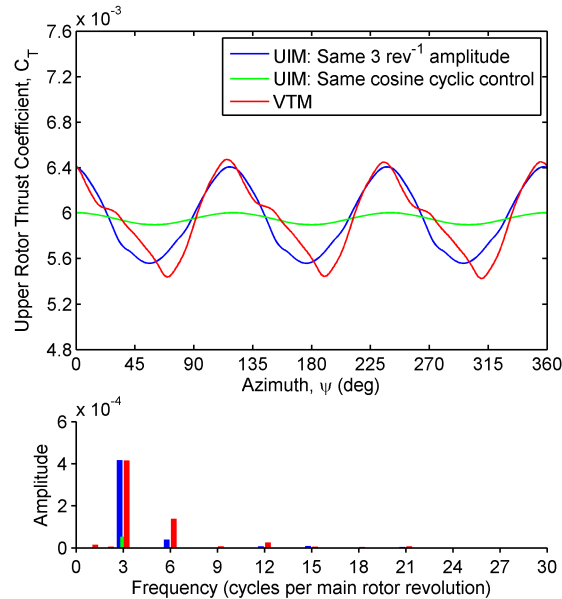


Figure 4.11: Comparison between the thrust coefficient generated by the upper rotor obtained with the VMT and the UIM simulations and respective frequency spectrum.

The first case, corresponding to the green curve, was obtained by replicating the cyclic control inputs between the VTM and the UIM simulations. The 3 rev^{-1} component is still present in the thrust signal and is a direct consequence of the simultaneous action of the aerodynamics of the three blades. If, however, the cosine cyclic control input is increased such that the amplitude of the 3 rev^{-1} component is the same as that obtained with the VTM simulation then the 6 rev^{-1} component becomes significant in the thrust signal obtained with uniform inflow. The increase in amplitude of the cosine cyclic input can thus mimic an aerodynamic interaction between the upper rotor and the vortex system trailed from the main rotor blades. The 6 rev^{-1} variation in thrust is not only attributable to the tip-vortices but also to the blade over-passage type of interaction. Both the 3 rev^{-1} and the 6 rev^{-1} variations of the thrust have a

marked increase in amplitude for the lower rotor.

The variation of power and pitching moment coefficients with azimuth of the isolated main rotor is given in appendix as figures A.4 and A.5. Although the mean power consumed by both the upper and lower rotors is the same, as to achieve yaw equilibrium, the power coefficient reveals high unsteadiness that is stronger for the lower rotor, where the amplitudes of the 9 and 12 rev^{-1} components of the frequency spectrum are higher than that of the 6 rev^{-1} .

The only significant variations of the pitching moment produced by the upper rotor have frequencies of 3 and 6 rev^{-1} only, as opposed to the lower rotor that shows the characteristic frequencies multiples of three, with 3, 9 and 15 the most significant ones. This is also an effect of the interference between the complex system of tip vortices produced by the main rotor and the blades of the lower rotor. It can be verified that the 6 rev^{-1} component is now stronger for the upper rotor.

4.3 Coaxial Rotor with Auxiliary Propulsor

This section treats the aerodynamic interactions that take place when the auxiliary propulsor is included in the coaxial rotor configuration discussed in the previous section. The interference effects on the main rotor induced by the propulsor are expected to be not as much pronounced as the interference effects induced by the main rotor into the propulsor, since the auxiliary propulsor is located far downstream of the main rotor. Indeed, the geometry of the wake, as well as the trajectory of the tip and root vortices from the main rotor are only slightly modified in the region of space upstream of the auxiliary propulsor, as can be verified when comparing figures 4.8 and 4.12.

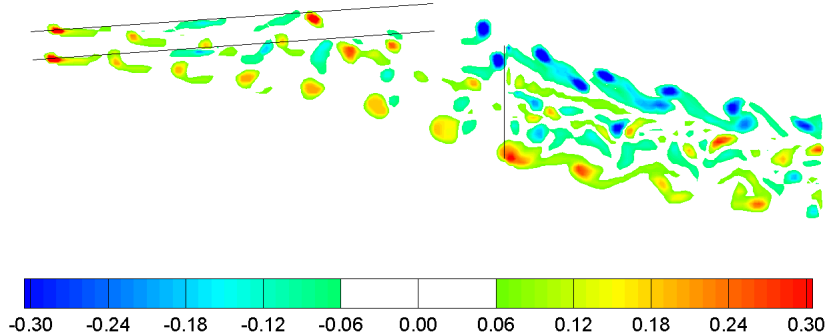


Figure 4.12: Contour plot of the y -component of non-dimensional vorticity (normalized by its maximum value ζ_{max}) in the $x - z$ plane for the configuration composed of the main rotor and auxiliary propulsor. Region of $|\zeta_y/\zeta_{max}| < 0.06$ not plotted for clarity.

Moreover, the aerodynamic environment of the main rotor when acting together with the auxiliary propulsor presents similar characteristics as those of the isolated main rotor, as can be seen in figure A.9, given in appendix, which shows a polar plot of the inflow velocity over a representative blade of the upper and lower rotors as a function of blade azimuth. The thrust, power and pitching moment coefficients produced by the main rotor as a function of blade azimuth are provided in the appendix under the figures A.10, A.11 and A.12, respectively, and are consistent with the observation that the main rotor aerodynamic environment is not much influenced with the introduction of the auxiliary propulsor.

There is, however, consequences in the loads generated by the main rotor that can be translated into an 1.8% decrease and 2.3% increase in the mean thrust produced by the upper and lower rotors, respectively, during one complete rotor revolution. Thus, instead of the 1.8% obtained for the isolated main rotor, the lower rotor now generates 6% more thrust than the upper rotor, as can be deducted from table A.2. This increase in the difference between the mean thrust produced by the upper and lower rotors is performed by the trim algorithm in order to counteract the yawing moment introduced by the auxiliary propulsor into the system.

The introduction of this yawing moment by the propulsor also manifests as a penalty in the power consumption of the system, which translates into a 1.6% increase in the power consumed by the main rotor. This increase is the result of a 3.9% increase in the power consumption of the lower rotor and only a slight decrease of 0.7% in the power consumption of the upper rotor.

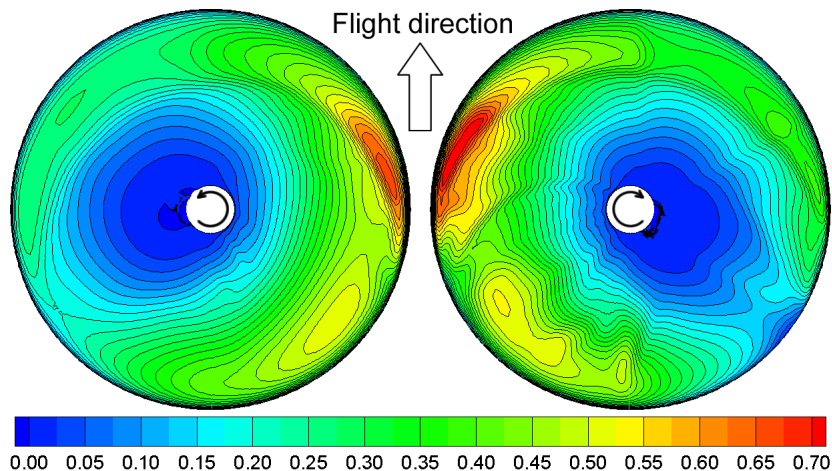


Figure 4.13: Distribution of loading over the blades of the upper and lower rotors during a complete rotor revolution for the configuration comprised of the main rotor and auxiliary propulsor. Left: upper rotor. Right: lower rotor.

The nose-up pitching moment introduced by the propulsor triggers the trim algorithm to respond by decreasing the nose-up pitching moment of the lower rotor and increasing significantly the nose-down pitching moment of the upper rotor. This is well patent in figure 4.13 that shows the blade loading distribution of the upper and lower rotors over one rotor revolution. There is a marked decrease in the concentration of blade loading in the upper half of the upper rotor disk as well as an increase on the lower half of the lower rotor disk relative to the isolated main rotor configuration.

Although the aerodynamic characteristics of the main rotor are not much disturbed by the inclusion of the auxiliary propulsor, the main rotor causes a strong effect on the aerodynamic environment of the auxiliary propulsor. The wake generated by the main rotor is convected past the propulsor, as depicted in figures 4.4 and 4.12, and modifies significantly the velocity field at the propulsor disk.

A clear evidence of the aerodynamic interaction between the main rotor wake and the propulsor is the skew of the propulsor wake. When acting alone, the propulsor generates a steady cylindrical wake characteristic of a propeller, as shown in figure A.22(a). However, when operating together with the main rotor, its wake is skewed downwards due to the downwash from the main rotor wake. According to figure 4.12, the tip vortices trailed by the main rotor blades pass through the propulsor and along its wake hence inducing rotation in the flow field near the upper and lower edge of the propulsor wake, which gives rise to the wave-like pattern that can be visualised in figure A.22(b). The root vortices also manifest in a way that is not so clear, as they seem to disrupt as they pass across the propulsor disk and then tend to roll-up with the propulsor wake.

The induced effects of the root-vortices as well as the tip-vortices on the inflow velocity field of the propulsor can be visualized in figure 4.14, which shows the mean and Root Mean Square (RMS) components of the inflow distribution over a representative blade. The method of decomposing the inflow distribution, or a periodic aerodynamic property in general, into the mean and RMS fluctuations as well as the reason why it is presented in this way is explained in appendix A.7.

The mean loading distribution constitutes a marked departure from the pattern that is expected when the propulsor is operated in isolation, as can be seen in figures A.6 and A.7 in appendix. Alone the propulsor loading distribution is similar to that of an hovering rotor. However, the downwash from the main rotor modifies the velocity field near the propulsor in such a way that, in the mean, the propulsor loading distribution becomes similar to that of a rigid rotor in forward flight. The heavy loaded advancing side of the rotor disk is a

prominent feature. It leads to the aforementioned yawing moment applied to the helicopter that is counteracted by the main coaxial rotor leading to higher overall power consumption.

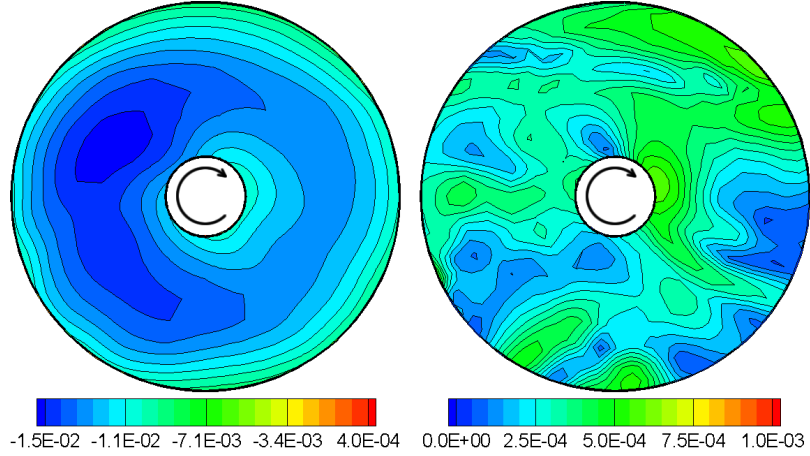


Figure 4.14: Distribution of inflow over the blades of the auxiliary propulsor as seen from behind the helicopter when operating together with the main rotor. Left: mean inflow. Right: RMS fluctuation in inflow.

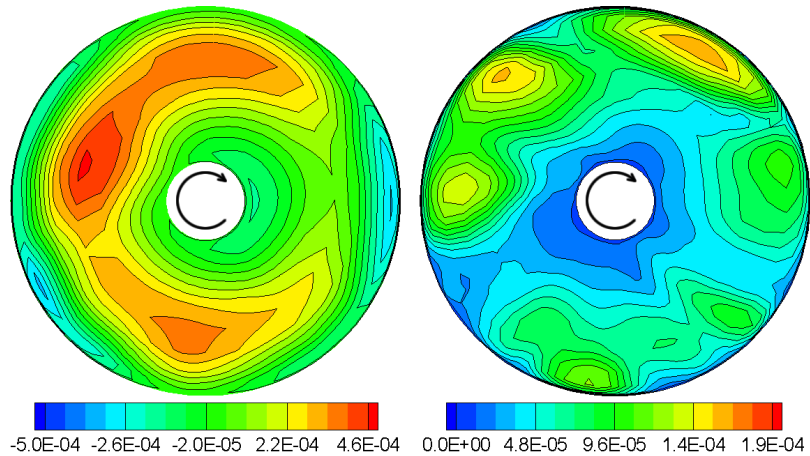


Figure 4.15: Distribution of blade loading over a representative blade of the auxiliary propulsor as seen from behind the helicopter when operating together with the main rotor. Left: mean loading. Right: RMS fluctuation in loading.

The localized patches of higher RMS fluctuation in the inflow distribution correspond to the regions of higher unsteadiness in the velocity field at the propulsor disk. This unsteadiness is a direct consequence of the passage of the tip and root vortices from the main rotor across these regions. Thus, the leading and trailing edge regions of higher inflow fluctuation can be associated

with the passage of tip vortices while the central, slightly biased to the right-hand side, as well as the smaller left-hand side regions of higher fluctuations can be associated with the impingement of root vortices.

The fluctuations that are observed in the inflow field on the auxiliary propulsor will alter the effective angle of attack of the blades hence introducing unsteadiness in the aerodynamic blade loading, as can be seen in figure 4.15. The fluctuation in blade loading is responsible for high vibration that is transmitted to the fuselage and also for high levels of noise. This is well patent in figure 4.16 that shows the thrust coefficient generated by the propulsor as a function of main rotor azimuth. Figures A.13 and A.14, provided in appendix, show the effects of this interaction on the power and pitching moment of the propulsor.

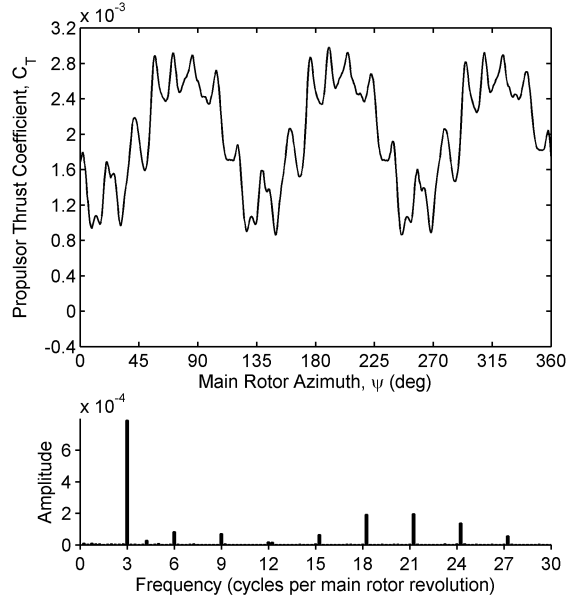


Figure 4.16: Thrust coefficient generated by the auxiliary propulsor over a complete main rotor revolution as a function of main rotor azimuth and respective frequency spectrum. (Thrust coefficient defined on the basis of the rotational speed, Ω_p , and radius, R_p , of the auxiliary propulsor.

The induced aerodynamic effect by the propulsor wake on the propulsor itself is reflected in the 21.25 rev^{-1} frequency, since the auxiliary propulsor is composed of 5 blades and rotates at 4.25 times faster than the main rotor. However, the frequency spectrum of figure 4.16 also shows a 3 rev^{-1} component of very high amplitude relative to the other components, and also smaller 6 and 9 rev^{-1} components that arise due to the interaction between the main rotor wake and the auxiliary propulsor. The amplitude of the 3 rev^{-1} compo-

ment of the thrust variation is approximately 40% of the mean thrust produced by the propulsor. Such high amplitude is associated with the large fluctuations in the velocity field that are caused by the series of tip vortices from the main rotor that pass across the propulsor disk. This high amplitude is also a consequence of the particular relative arrangement between the series of upper and lower rotor tip vortices in the wake of the main rotor. This pattern is dependent on the particular phasing between the upper and lower rotors. In the configuration presented here the blades of the upper and lower rotors pass over each other at zero azimuth angle, which corresponds to the rear of the respective disks. Hence, the tip vortices that are generated by those blades are convected very close to each other forming a coherent structure as they pass the propulsor disk. If the phasing of the main rotor disks were changed such that the blades of the upper and lower rotors pass over each other at a different azimuth angle, a different pattern of wake tip vortices would be obtained, as depicted in figures A.1 and A.2 in appendix, which could modify the amplitude of the 3 and 6 rev^{-1} components of the thrust coefficient.

4.4 Complete Configuration

This section presents the results obtained with the complete or full helicopter configuration, which is comprised of the main rotor, auxiliary propulsor, fuselage and tailplane. The role of the fuselage in modifying the wake from the main rotor was explained previously in section 4.1. The trajectory of the tip vortices is displaced significantly due to an indirect interaction with the fuselage, as can be seen in figure 4.17.

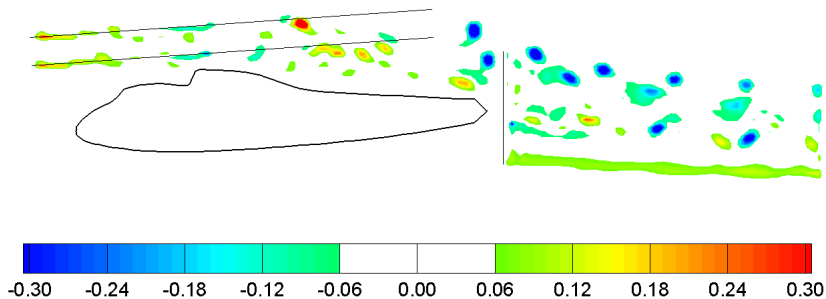


Figure 4.17: Contour plot of the y -component of non-dimensional vorticity (normalized by its maximum value ζ_{max}) in the $x - z$ plane for the complete configuration. Region of $|\zeta_y/\zeta_{max}| < 0.06$ not plotted for clarity.

This upwards deflection of the wake forces the trailed vortices from the upper and lower rotors to remain closer to the respective rotor plane which trans-

lates into a marked modification in the strengths of the localized radial gradients of inflow, as can be visualized by comparing the inflow distribution of the previous configuration with the complete configuration, figures A.9 and A.16. It is also visible that the full configuration presents a wider region of upflow on the forward half of the disk and specially through the lower rotor and that this upflow is higher than for the configuration without the fuselage. The fuselage also contributes to an increase in downflow through the rear half of the upper and lower rotor. This might be better grasped through figure 4.18, that was obtained by computing the difference between the inflow distribution of both configurations.

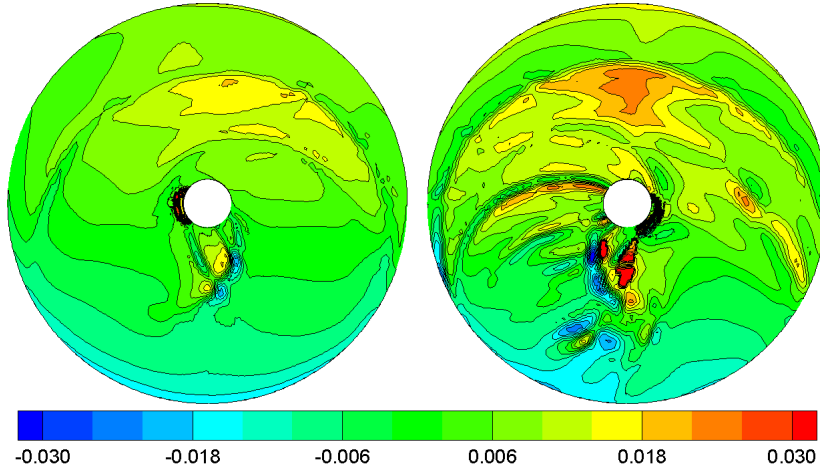


Figure 4.18: Distribution of the difference in inflow between the complete configuration and that comprised of the main rotor and auxiliary propulsor. Left: upper rotor. Right: lower rotor.

It is apparent that the difference over the forward part of both rotor disks is generally positive and that over the rear part is generally negative. However, this difference in the longitudinal gradient of inflow is not only induced by the presence of the fuselage but is also a result of the modification of inflow that is a consequence of the redistribution of blade loading performed by the trim algorithm in order to counteract the strong nose-up pitching moment on the helicopter that is induced by the downwash on the tailplane. In other words, the impingement of the main rotor wake into the upper surface of the tailplane creates a download there, which in turn generates a nose-up pitching moment about the centre of gravity of the helicopter. This aerodynamic interaction between the main rotor wake and the horizontal tailplane is known as 'pitch-up' and has caused significant problems in flight dynamics and control that hampered the development of helicopters in the past decades, Ref. [42].

In order to maintain the equilibrium of the system, longitudinal cyclic pitch

is fed into the blades of the main rotor in such a way that enough nose-down pitching moment is produced. Results show that the mean nose-down pitching moment produced by the main rotor when operating in the full configuration is approximately 9.4 times that when operating without the inclusion of the fuselage and tailplane. Figure 4.19 provides a better insight into this aerodynamic interaction between the tailplane and the main rotor. It was obtained by the difference between the blade loading distribution that is presented in figures A.17 and 4.13. This figure reflects how the blade loading is redistributed in order to produce the required pitching moment in the system. It is apparent that the blades become less loaded at the forward part of both rotors and more loaded in the rear part. However the decrease in blade loading over the forward part and the increase in blade loading over the rear part is far more marked in the lower and upper rotors respectively. The pitching moment coefficient generated by the upper and lower rotors as a function of blade azimuth is presented in figure A.19, given in appendix, and shows a shift in the mean pitching moment generated by both rotors towards more negative values relative to the configuration where the fuselage and tailplane are absent, which is in agreement with the previous results. Comparison with the frequency spectrum of figure A.12 shows a change in the amplitude of the 3 and 6 rev^{-1} components, although similar characteristics in the frequency content are apparent.

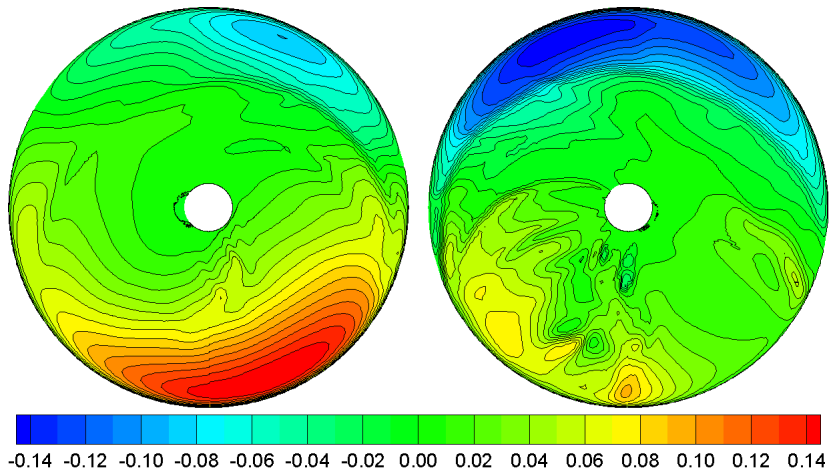


Figure 4.19: Distribution of the difference in blade loading between the complete configuration and that comprised of the main rotor and auxiliary propulsor. Left: upper rotor. Right: lower rotor.

Figure 4.20 shows the variation, over one main rotor revolution, of the thrust generated by the upper and lower rotors of the coaxial system. It can be observed that the frequency characteristics of the thrust curve are similar to the previous configurations, with the usual dominant 3 and 6 rev^{-1} components

that were introduced in section 4.2. However, comparison with the configuration where the fuselage and tailplane are absent, shows an increase of the mean thrust, over one rotor revolution, that is produced by the upper rotor while the lower rotor mean thrust is not significantly altered. This is also evident in the values for the thrust coefficient provided in tables A.2 and A.3, which reveal a 13% increase and a 0.7% decrease in the mean thrust produced by the upper and lower rotors, respectively. This extra thrust generated by the upper rotor is required to ensure the overall vertical force equilibrium in the system and arises when the fuselage and tailplane are included in the helicopter configuration.

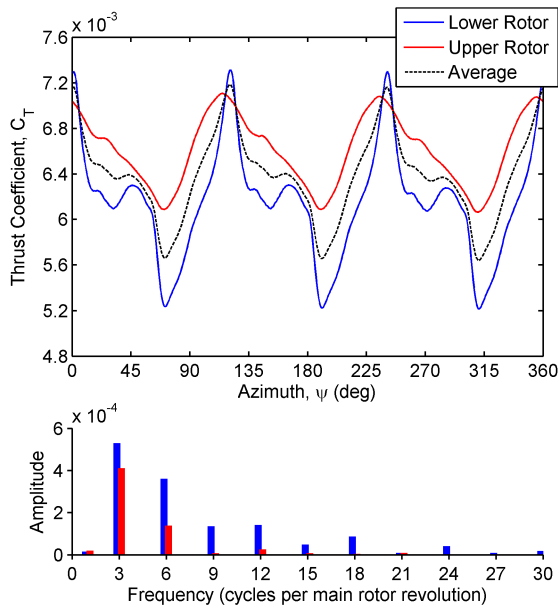


Figure 4.20: Thrust coefficient generated by the upper and lower rotors of the coaxial system as a function of azimuth and respective frequency spectrum for the complete configuration.

Hence, the fuselage and mainly the tailplane are responsible for a downward force that is due to the impingement of the main rotor wake into the upper surface of these components. The reason why the increase in mean thrust is associated with the upper rotor is because of the trim methodology employed in the simulation, which is explained in section 2.8. Indeed, the trim algorithm increases the collective pitch of both the upper and lower rotors by the same amount, which causes the thrust produced by both rotors to increase, at least approximately, by the same amount, but simultaneously it increases the difference in collective pitch between the upper and lower rotors in order to trim the mean yawing moment of the system. Since the yawing moment that results from the inclusion of the fuselage and tailplane is in the positive z -axis

direction, the upper rotor torque must also be increased. This iterative process results in the marked increase of the mean thrust produced by the upper rotor and small or insignificant change in that produced by the lower rotor.

Figure 4.20 also shows an increase in the 6 rev^{-1} component of the thrust signal for the lower rotor relative to the configuration where the fuselage and tailplane are absent. This is indicative of the stronger blade-vortex interactions that result from the blade over-passage between the upper and lower rotors.

Figure A.18, given in appendix, compares the variation in the power consumed by the upper and lower rotors with azimuth, over one rotor revolution. Again, the same frequency characteristics are observed between the different configurations although the amplitudes of the various components vary considerably. With the inclusion of the fuselage and tailplane into the configuration, the power consumed by the lower rotor increases 3% whereas that consumed by the upper rotor increases 15%, which is an effect of the increase in the thrust and torque produced by the upper rotor in order to balance the download and yawing moment, respectively, introduced by the fuselage and tailplane.

The interference effects brought in by the introduction of the fuselage and tailplane into the configuration also extend to the auxiliary propulsor. Since the main rotor shaft has 4° of forward tilt, the increase in the mean thrust produced by the upper rotor not only results in a higher lift generated by the main rotor system but also in a larger propulsive force. The method used to trim the rotorcraft responds to this increment by decreasing the propulsive thrust generated by the auxiliary propulsor. Indeed, tables A.2 and A.3 show a 33% decrease in thrust produced by the propulsor and, consequently, a 16% reduction in the power consumption relative to the configuration where the fuselage and tailplane were not included.

The aerodynamic interaction between the main rotor wake and the propulsor wake is also modified with the inclusion of the fuselage and tailplane. After comparing figures 4.12 and 4.17, it can be inferred that the main rotor wake is constrained to convect downwards by the presence of the fuselage and so is compelled to affect a smaller portion of the propulsor disk, which corresponds to its upper half. Consequently, figure A.22(c) shows that the upper half of the propulsor wake still presents the wave-like pattern that is visible in figure A.22(b). However, the lower half of the propulsor wake presents a more uniform geometry that closely resembles that of figure A.22(a) where the propulsor is operating in isolation.

Figure 4.21 shows the mean and RMS fluctuation in the blade loading over the propulsor disk, which is in close agreement with the results for the wake geometry given in figure A.22(c). It can be observed that the lower region of the propulsor disk presents smaller fluctuations in blade loading relative to the

configuration without the fuselage, figure 4.15.

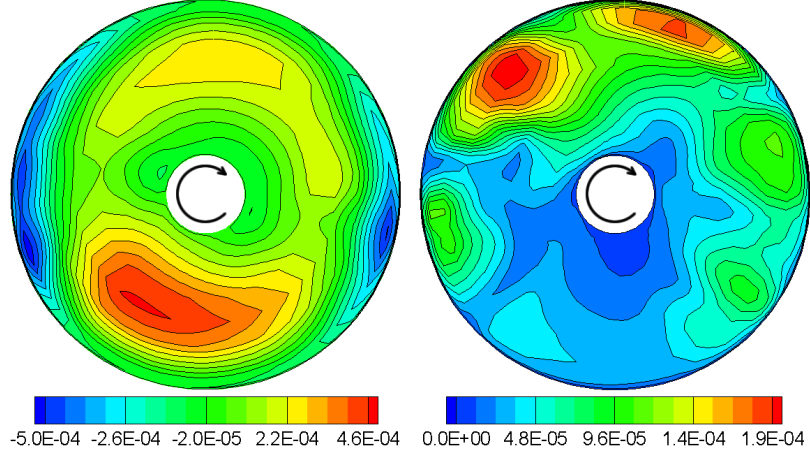


Figure 4.21: Distribution of blade loading over a representative blade of the auxiliary propulsor as seen from behind for the complete configuration. Left: mean loading. Right: RMS fluctuation in loading.

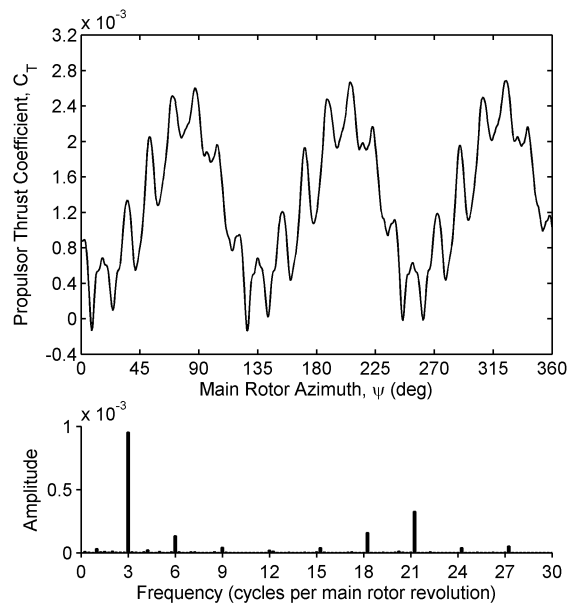


Figure 4.22: Thrust coefficient generated by the auxiliary propulsor over a complete main rotor revolution as a function of main rotor azimuth and respective frequency spectrum for the complete configuration. (Thrust coefficient defined on the basis of the rotational speed, Ω_p , and radius, R_p , of the auxiliary propulsor.

The upper region of the propulsor disk presents patches of RMS fluctuation that correspond to the regions where the vortices from the main rotor cross the

plane of the propulsor. Comparison with figure 4.15 shows that the amplitude of the RMS fluctuation of these patches increases slightly when the propulsor is integrated into the full configuration. This is in agreement with figure 4.22 that also reveals an increase in the amplitude of the 3 rev^{-1} component of the thrust produced by the propulsor. This can be attributable to an increase in the strength of the trailed vorticity from the blades of the upper rotor that is related to the increase in the upper rotor aerodynamic loading alluded to earlier.

The power consumed by the propulsor as a function of main rotor azimuth is provided in appendix, figure A.20, and shows very similar frequency characteristics to the variation in thrust in figure 4.22. It can be seen the expected reduction in the time averaged or mean power consumed and an increase in the amplitude of the 3 rev^{-1} component, relative to the configuration without fuselage and tailplane.

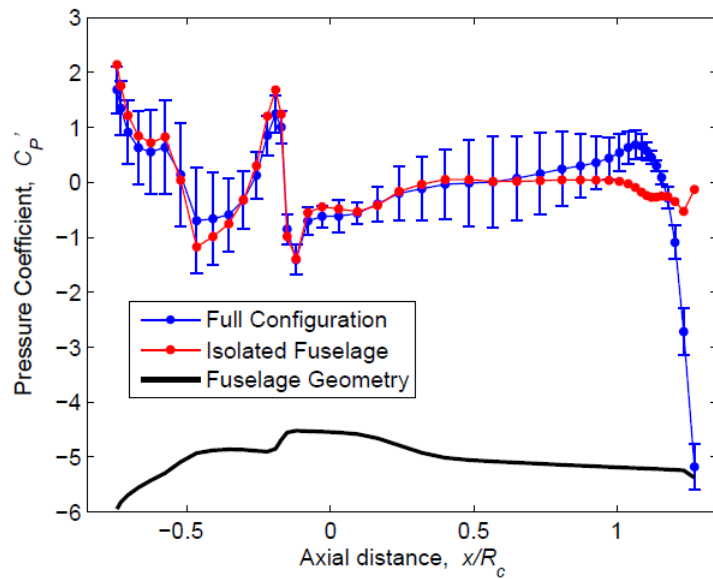


Figure 4.23: Variation of the time averaged pressure coefficient along the top centreline of the fuselage. (Error bars represent the amplitude of the RMS fluctuations in the pressure signal obtained for the full configuration. *Courtesy of Dr. H. Kim and Dr. A. Kenyon.*)

Figure 4.23 shows the variation of the mean modified pressure coefficient along the top centreline of the fuselage, in other words, along the upper half of the curve obtained by the intersection of the $x - z$ plane with the fuselage

surface. This figure compares the pressure distribution along the fuselage that was obtained for two distinct cases. In the first case, the full configuration was flown at advance ratio $\mu = 0.15$. In the second case, every component attached to the fuselage was removed and the fuselage was flown at the same free-stream velocity as in the first case.

The trajectory of the tip vortices that trail from the main rotor system, depicted in figure 4.17, show that the main rotor wake passes very close to the rear of the fuselage. The downwash velocity it induces on that part of the fuselage is thus responsible for the increase in the mean component of pressure over that region, as can be seen in figure 4.23. This direct interaction between the main rotor wake and the fuselage is expected to be highly dependent in the advance ratio, however, becoming more pronounced for lower advance ratios as the wake is allowed to convect close to a larger portion of the fuselage.

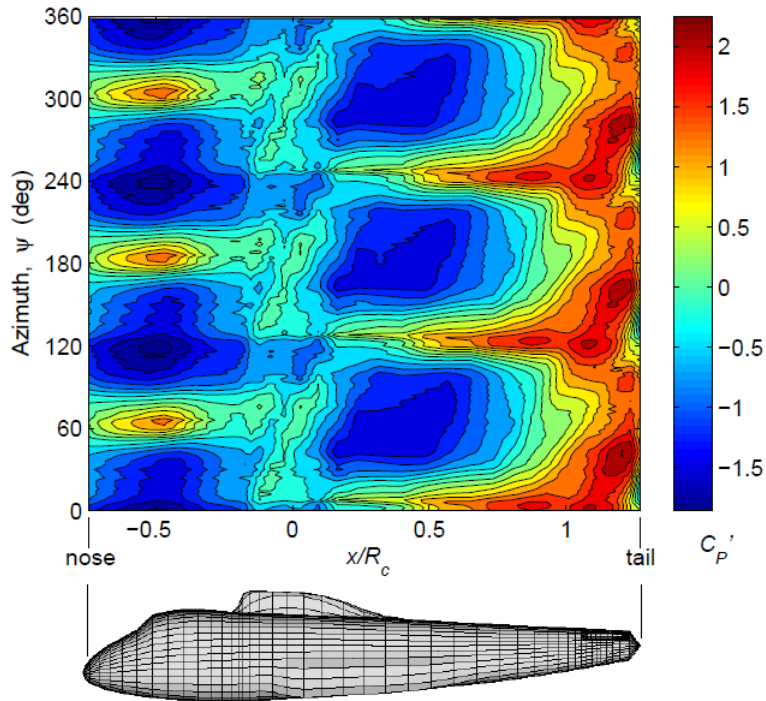


Figure 4.24: Contours of the unsteady pressure component along the top centreline as a function of main rotor azimuth obtained for the full configuration. Mean component of the signal removed. (*Courtesy of Dr. H. Kim and Dr. A. Kenyon.*)

Other notorious feature presented in figure 4.23 is the significant fluctuations in the pressure variation. These fluctuations are more pronounced in two regions – one at the front of the fuselage, from the nose until about $x/R_c = -0.2$,

and the other between $x/R_c = 0.2$ and $x/R_c = 1.0$. In order to better grasp the origins of these fluctuations, figure 4.24 shows a contour plot of the VTM-predicted unsteady component of the pressure, $\partial\phi/\partial t$, along the top centreline of the fuselage as a function of azimuth, at an advance ratio of $\mu = 0.15$. This figure is in agreement with figure 4.23 since the regions of higher fluctuation in the pressure distribution are strongly correlated. Thus, both regions of higher pressure fluctuations are characterised by patches of elevated over-pressure followed by patches of elevated suction. The patches of elevated pressure, however, have shorter time duration than those of elevated suction and occur almost instantaneously and at a frequency of 3 rev^{-1} . However, the pressure fluctuation at the region between the nose and about $x/R_c = -0.2$ presents a 60° of phase shift relative to the pressure fluctuation at the region from $x/R_c = 0.2$ and $x/R_c = 1.0$. Moreover, both regions are located directly below the area swept by the main rotor blades. It may be inferred from these features that the strong fluctuation in the pressure distribution over these regions is an effect of the periodic close passage of the blades over the fuselage. The blades are responsible for generating a strong bound vortex that is capable of modifying the velocity field in the vicinity of the fuselage upper surface which in turn will affect the pressure distribution. The dominant 3 rev^{-1} frequency that is characteristic of the blade close-passage event would be modified if the phasing between the blades of the upper and lower rotors was altered. In that case, the blades would not overlap when passing directly above the top centreline of the fuselage which would result in the unsteady pressure signal presenting a dominant 6 rev^{-1} frequency.

The unsteady pressure signature over the region from about $x/R_c = 0.2$ and $x/R_c = 1.0$ is a result of the combined effects of the blade close-passage and a secondary, less marked event that consists in the close-passage of the individual vortices that are trailed from the main rotor. The convection of these individual vortices continues downstream over the remainder of the fuselage. From about $x/R_c = 1.0$ until just short of the tail the effects of the blade close-passage tend to cease while the effects of these individual vortices become more significant as they gradually approach the surface of the fuselage. Indeed, this feature can be identified as a series of travelling waves that are represented in figure 4.24 by the diagonal contours over the region from about $x/R_c = 1.0$ until just short of the tail.

5 CONCLUSION

The physical processes that govern the aerodynamic interactions and flow phenomena of a compound coaxial helicopter model have been investigated computationally. The helicopter model employed in this study is representative of a generic modern helicopter that exploit the Advancing Blade Concept. This concept features two rotors arranged in a coaxial configuration and rotating in opposite directions. The blades of each rotor are very stiff and are rigidly attached to the hub allowing for a minimized inter-rotor separation. The helicopter model is also compounded in propulsive thrust with the addition of a pusher propeller mounted at the rear of the fuselage.

The detailed geometric and aerodynamic characteristics of this particular model were not designed with the purpose of epitomising any particular real life helicopter, but to be representative of prototypes that employed the ABC rotor, like the Sikorsky's X2 or the XH-59A technology demonstrators. Therefore, the results presented here lack from a source of proper experimental data and ought to be validated. However, the numerical model used to arrive to these results was validated previously against several reliable experimental data sets corresponding to different helicopter configurations and for several flight conditions. The results obtained provided good evidence that the coupled lifting-line – VTM model gives an accurate prediction of the evolution of the main rotor wake. The key feature of this model is its ability to preserve the integrity of the vortical structures of the wake many rotor radii downstream of its source, using less computational resources than standard CFD methods, [15]. This is indeed an important aspect when modelling aerodynamic interactions in helicopters since in one hand the primary contributor to the unsteady aerodynamic forcing of the vehicle is the interaction between the wake induced by the main rotor and the other components of the vehicle. In the other hand, the wake induced effects depend on the vorticity field of the wake even at locations far downstream of the rotors.

As such, the previous validation of the lifting-line – VTM model showed that it is capable of predicting the wake geometry and its evolution process, blade-vortex interactions, rotor vibration and other interactional phenomena. Thus, it is well suited for the analysis of aerodynamic interactions of helicopters, which grows confidence in the qualitative accuracy of the results presented here. However, the prediction of essentially viscous phenomena, like boundary

layer separation, is beyond the capabilities of the current model. Therefore, some significant discrepancies are to be expected near the blades of the rotors. Hence, flow separation within the blades relies on the accuracy of the airfoil data that is used in the pre-computation of the lift as a function of angle of attack on each blade panel. Moreover, boundary layer separation may occur at the fuselage surface causing secondary vortices to appear close to the surface.

The VTM also does not directly account for the compressibility of the flow and relies on the quality of the airfoil data or in the accuracy of the Prandtl compressibility correction.

Another indubitable source of inaccuracy in the results stems from the omission of the hubs of the main rotor and auxiliary propulsor. These components could further distort and potentially disrupt the vortical structures of the main rotor wake, thus introducing an additional source of unsteadiness into the system. Vortex shedding from the hub and the interaction between the wake and the fuselage boundary layer are believed to be partly responsible for the high frequency content of the pressure distribution at the rear of the fuselage top centreline, [34].

The numerical results presented here were obtained for different helicopter configurations and subsequently analysed in the light of the reductionist approach adapted from the work of Sheridan and Smith, [12]. This method relies on the direct comparison between the different configurations in order to track the source or cause of perturbations in the velocity field and forces of the more complex full helicopter model. However, this method presents some deficiencies due to the fact that the main rotor reacts very differently to this perturbations for each configuration tested and in a way that is not yet fully understood. For instance, the inclusion of the fuselage led to the upwards displacement of the wake which in turn induced an upflow at the forward part and a downflow at the rear part of the upper and lower rotor disks. Nonetheless, this interaction is somewhat obscured by the surge in the longitudinal gradient of inflow that is caused by the main rotor trim algorithm that tries to even out the pitching moment imbalance that is generated by the download on the tailplane. Thus, some aerodynamic interactions can manifest simultaneously and may be characterised by constructive or destructive interference between two or more components. The fact that the main rotor is trimmed in order to achieve force and moment equilibrium may also contribute to this imbroglio because the trimming mechanism inherently leads to complex feedback loops that enshroud some aerodynamic interactions and make it difficult to isolate the effects induced by different components of the vehicle. These feedback loops continue to happen even after equilibrium is achieved, in a time average sense, and are characterised by the gradual adjustment of the vorticity field

and the loads on the various components of the system. In order to gain a deeper understanding of what caused and what are the consequences of the different aerodynamic interactions that were identified, it is suggested that this study should be complemented with results obtained from the numeric simulation of the different configurations in a wind tunnel, i.e. without rotor trimming, and at the same advance ratio. The collective and cyclic pitch inputs could then be used as simulation parameters that could be varied between different runs. Moreover, another intermediate stage should be introduced in this building-block approach that consists in the complete configuration with only the tailplane removed, since it could better isolate the interactional effects between the wake, fuselage and tailplane.

A range of aerodynamic interactional phenomena was identified and characterised for this generic helicopter model, at the advance ratio of $\mu = 0.15$. The following conclusions can be drawn from the results of the present work:

- The main rotor is responsible for the generation of strong tip and root vortices that are convected downstream. The tip vortices from the upper and lower rotors interact with each other and tend to roll-up and merge into a pair of concentrated vortex structures or super-vortices.
- The distribution of vorticity in the wake of the main rotor is asymmetric with respect to the $x - z$ plane. It was verified that the trajectory of the elements of the root vortex system was biased to the port side of the vehicle for all the configurations tested and that the propulsor wake trajectory also presented a slight skew towards that side. It may be inferred that the concentration of vorticity in the super vortex of the port side is higher than in the starboard side. This asymmetry is consistent with the stronger vorticity trailed from the left hand side of the coaxial system, which in turn is dependent on the distribution of blade loading required to trim the system.
- Due to the proximity to the starboard tip vortex, the trajectory of the vortex trailed from the starboard tip of the tailplane is biased towards the right hand side. In the other hand, the vortex trailed from the port side tip of the tailplane together with the root vortices from the main rotor, are completely entrained in the wake generated by the auxiliary propulsor.
- From the $x - z$ cross section of the vorticity distribution in the main rotor wake, it was verified that the wake skew angle is higher in the complete configuration than for the configuration without fuselage. This interaction is explained by the displacement of the velocity field in the vicinity of the main rotor that is induced by the fuselage. The fuselage forces the flow

around it, thus inducing an upflow in the region over the top surface starting from the nose until roughly $x/R_c = -0.4$. Over the top surface of the rear part of the fuselage the flow experience the opposite effect, i.e. a downflow.

- The difference in the skew angle between the wakes generated by the isolated main rotor and the combined main rotor and auxiliary propulsor was not significant. This is because the propulsor wake is quickly convected downstream of the vehicle and hence its direct interaction with the velocity field around the main rotor is very weak. Nonetheless, the propulsor wake is entrained in the main rotor wake and so interacts with it, modifying the vorticity distribution. As a result, the modified vorticity field in the far wake feeds back into the velocity field surrounding the main rotor, which in turn will have an impact in the inflow distribution over the upper and lower rotor disks. Although the precise characterisation of the signature left by this indirect interaction in the inflow distribution of the main rotor is difficult to ascertain due to the simultaneous action of the trim mechanism in altering the blade loading distribution over its blades.
- The inflow velocity field over the upper and lower rotors is characterised by a longitudinal gradient over the whole rotor disks and several high localised gradients that are identified by curved ridges in the contour plot of the inflow distribution over the rotor disks. The longitudinal gradient describes the variation of inflow that is required in order to achieve moment equilibrium of the system and begins with an upwash at the leading edge, changes to downwash after the first curved ridge and continues towards the trailing edge where the intensity of the downwash is higher. The strong localised gradients of inflow represent the induced effects of the trailed vortex structures produced by the rotating blades as they pass close to the rotor plane. The curved ridges on the lower rotor outnumber those on the upper rotor because the tip vortices from the upper rotor are convected towards the lower rotor and add up to the tip vortices that were generated by the lower rotor. Hence, the influence of the upper rotor in modifying the inflow distribution of the lower is more significant than the converse. These strong gradients constitute powerful BVI's that are capable of fomenting unsteadiness in the blade loading variation which translates into vibration and noise.
- The variation of thrust produced and power consumed by the main rotor with azimuth revealed high unsteadiness with frequencies that are multiple of 3 rev^{-1} . The dominant frequency of the thrust and power signals was the 3 rev^{-1} that is not only a direct effect of the blade-vortex

interaction but is also a consequence of the aerodynamic properties of the blades. The amplitude of the 6 rev^{-1} component also contributed significantly for the unsteadiness of the thrust variation. This frequency correlates with the six radial ridges that are visible in the inflow distribution over the lower rotor disk and are a manifestation of the blade overpassage type of interaction. However, the VTM replaces each blade by a bound vortex that acts as a source inside the computational domain and thus the influence of the blade geometry on the upwash-downwash effect is not modelled directly. The VTM is not capable of predicting another 6 rev^{-1} phenomenon that depends on the geometry of the blades and is known as the Venturi effect, Ref. [43]. It is caused by the thickness of the blades and manifests as a reduction in pressure between the overlapping blades.

- The high amplitude of the 3 rev^{-1} component of the propulsor thrust variation indicates a powerful interaction between the main rotor wake and propulsor that consists of the ingestion of main rotor tip vortices by the propulsor. This causes the propulsor to act as a strong source of dynamic excitation in the fuselage, mainly due to the unsteady force directed along the x -axis but also in pitch and roll. Although this excitation might be ameliorated if the phasing of the upper and lower rotors is changed. The propulsor wake interacts with the propulsor blades at a higher frequency of 21.25 rev^{-1} , although at lower amplitude than the 3 rev^{-1} component.
- The inclusion of the fuselage and tailplane in the model resulted in a increase in the longitudinal gradient of inflow, and a redistribution of blade loading over the upper and lower rotors such that the mean nose-down pitching moment produced by the main rotor became approximately 9.4 times greater than that obtained without the fuselage and tailplane. This nose-down pitching moment is required to balance the nose-up pitching moment that is mainly a consequence of the download in the tailplane. This down-force in the tailplane is a direct result of the aerodynamic interaction between the main rotor wake and tailplane and manifests itself in a flight dynamic phenomena known as 'pitch-up'. The magnitude of this download is dependent upon the specific geometry of the empennage, the position of the tailplane relative to the main rotor and the advance-ratio, Ref. [42].
- It was verified that the mean thrust produced by the upper rotor increased by 13% with the addition of the fuselage and tailplane. This increase appears in order to counteract the down-force that is produced by the

fuselage and tailplane and is a direct consequence of the aerodynamic interaction between those components and the main rotor wake. Since the main rotor is tilted forward, the propulsive force it generates is also increased, thus alleviating the loading of the auxiliary propulsor and leading to a reduction in its power consumption relative to the configuration without fuselage and tailplane. This side-effect is clearly non-optimal since the propulsor is consuming power without providing a significant contribution to the propulsion of the system (about 16.7% of the main rotor propulsive force).

- Significant fluctuations in the blade loading distribution over the auxiliary propulsor disk are induced by the ingestion of tip and root vortices from the main rotor. With the fuselage and tailplane present, the propulsor lower half become isolated from the vortex impingement and thus the fluctuations occur on the upper half. These fluctuations are dominated by a 3 rev^{-1} frequency due to the interaction with the main rotor wake. A 21.25 rev^{-1} frequency component of lower amplitude is also present and is due to the interaction with the tip vortices produced by the propulsor itself. The fluctuations in the blade loading may excite significant vibration to the aircraft.
- The aerodynamic interaction between the main rotor wake and the fuselage is responsible for a gross modification of the pressure forces over the fuselage surface. The impingement of the wake over the rear of the fuselage causes an increase in the mean pressure there. This effect, together with the download in the tailplane, contribute to the nose-up pitching moment about the aircraft centre of gravity, leading to the redistribution of loads over the main rotor blades alluded to earlier.
- Significant unsteadiness is experienced in the regions of the fuselage located directly below the main rotor blades. This unsteadiness is characterized by fluctuations with dominant frequency of 3 rev^{-1} and is associated with the passage of the blades over the fuselage. Although the main rotor is composed of 6 blades, they are arranged such that they overlap directly above the top centreline of the fuselage. Thus, if another phasing between the upper and lower rotors was adopted, a frequency of 6 rev^{-1} for the pressure fluctuations would be expected. The vortical structures produced by the main rotor convect very close to the top surface of the fuselage and constitute another source of unsteadiness in the pressure distribution from $x/R_c = 0.2$ until just short of the tail.

BIBLIOGRAPHY

- [1] Kim, H. W. and Brown, R. E., "Coaxial Rotor Performance and Wake Dynamics in Steady and Manoeuvring Flight," *Proceedings of the 62nd Annual Forum of the American Helicopter Society*, Phoenix, Arizona, May 2006.
- [2] Kim, H. W. and Brown, R. E., "Impact of Trim Strategy and Rotor Stiffness on Coaxial Rotor Performance," *Proceedings of the 1st AHS/KSASS International Forum on Rotorcraft Multidisciplinary Technology*, Seoul, Korea, Oct. 2007.
- [3] Curnock, D., *The Little Book of Flight*, Green Umbrella Publishing, 2008.
- [4] Leishman, J. G., *Principles of Helicopter Aerodynamics*, Cambridge University Press, Cambridge, UK, 2nd ed., 2006.
- [5] Newman, S. J., "The Compound Helicopter Configuration and the Helicopter Speed Trap," *Aircraft Engineering and Aerospace Technology: An International Journal*, Vol. 69, No. 5, 1997, pp. 407–413.
- [6] Johnston, J. F. and Cook, J. R., "AH-56A Vehicle Development," *American Helicopter Society 27th Annual Forum Proceedings*, Washington DC, USA, 1971.
- [7] Ruddell, A. J., "Advancing Blade Concept (ABC) Development," *Proceedings of the 32nd Annual National Forum of the American Helicopter Society*, Washington, D.C., May 1976.
- [8] Ruddell, A. J. and et al, "Advancing Blade Concept (ABC) Technology Demonstrator," Tech. Rep. USAAVRADCOM-TR-81-D-5, Sikorsky Aircraft Division of United Technologies Corporation, April 1981.
- [9] Paglino, V. M., "Forward Flight Performance of a Coaxial Rigid Rotor," *Proceedings of the 27th Annual National Forum of the American Helicopter Society*, Washington, D.C., May 1971.
- [10] M. C. Cheney, J., "The ABC Helicopter," *Presented at the AIAA/AHS VTOL Research, Design and Operations Meeting*, Atlanta, Ga., Feb. 1969.

- [11] Burgess, R. K., "Development of the ABC Rotor," *Proceedings of the 27th Annual National Forum of the American Helicopter Society*, Washington, D.C., May 1971.
- [12] Sheridan, P. F. and Smith, R. P., "Interactional Aerodynamics - A New Challenge to Helicopter Technology," *Journal of the American Helicopter Society*, Vol. 25, No. 1, 1980, pp. 3–21.
- [13] Fletcher, T. M. and Brown, R. E., "Main Rotor - Tail Rotor Interactions and Its Implications for Helicopter Directional Control," *Proceedings of the 32nd European Rotorcraft Forum*, Maastricht, Netherlands, 2006.
- [14] Hariharan, N., "A Review of Computational Techniques for Rotor Wake Modeling," *Journal of the American Institute of Aeronautics and Astronautics*, Vol. 1, No. 14, 2000.
- [15] Brown, R. E. and Line, A. J., "Efficient High-Resolution Wake Modeling Using the Vorticity Transport Equation," *Journal of the American Institute of Aeronautics and Astronautics*, Vol. 43, No. 7, July 2005, pp. 1434–1443.
- [16] Phelps, A. E. and Mineck, R. E., "Aerodynamic Characteristics of a Counter-Rotating, Coaxial, Hingeless Rotor Helicopter Model With Auxiliary Propulsion," TM 78705, NASA, May 1978.
- [17] Felker, F. F., "Performance and Loads Data from a Wind Tunnel Test of a Full-Scale, Coaxial, Hingeless Rotor Helicopter," TM 81329, NASA, Oct. 1981.
- [18] Bagai, A., "Aerodynamic Design of the Sikorsky X2 Technology Demonstrator Main Rotor Blade," *American Helicopter Society 64th Annual Forum*, Montréal, Canada, 29 April–1 May 2008.
- [19] Aris, R., *Vectors, Tensors, and the Basic Equations of Fluid Mechanics*, Dover, 1989.
- [20] Rosenhead, L., "The Spread of Vorticity in the Wake Behind a Cylinder," *Proceedings of the Royal Society of London*, Vol. 127, Nr. 806 of A, June 2, 1930, pp. 590–612.
- [21] Moore, D. W., "Finite Amplitude Waves on Aircraft Trailing Vortices," *Aeronautical Quarterly*, Vol. 23, 1972, pp. 307–314.
- [22] Weissinger, J., "The Lift Distribution of Swept-Back Wings," TM 1120, NACA, March 1947.

- [23] Ahlin, G. A., *The Fluid Dynamics of the Helicopter Vortex Ring Phenomenon*, Ph.D. thesis, Department of Aeronautics, Imperial College of Science, Technology and Medicine, London, U.K., 2004.
- [24] Kenyon, A. R., *Helicopter Rotor-Fuselage Interactions*, Ph.D. thesis, Department of Aeronautics, Imperial College of Science, Technology and Medicine, London, U.K., 2008.
- [25] Line, A. J., *Computational Modelling of Helicopter High-Frequency Dynamics*, Ph.D. thesis, Department of Aeronautics, Imperial College of Science, Technology and Medicine, London, U.K., 2007.
- [26] Dingeldein, R. C., “Wind-Tunnel Studies of the Performance of Multirotor Configurations,” TN 3236, NACA, Aug. 1954.
- [27] Paglino, V. M. and Beno, E. A., “Full-Scale Wind-Tunnel Investigation of the Advancing Blade Concept Rotor System,” Tech. Rep. USAAMRDL TR 71-25, Sikorsky Aircraft Division of United Aircraft Corporation, Aug. 1971.
- [28] Caradonna, F. X. and Tung, C., “Experimental and Analytical Studies of a Model Helicopter Rotor in Hover,” TM 81232, NASA, Sept. 1981.
- [29] Kocurek, J. D. and Tangler, J. L., “A Prescribed Wake Lifting Surface Hover Performance Analysis,” *Journal of the American Helicopter Society*, Vol. 21, No. 1, 1976, pp. 24–35.
- [30] Harris, F. D., “Articulated Rotor Blade Flapping Motion at Low Advance Ratios,” *Journal of the American Helicopter Society*, Vol. 17, No. 1, 1972, pp. 41–48.
- [31] Line, A. J. and Brown, R. E., “High Resolution Wake Modelling Using a Semi-Lagrangian Adaptive Grid Formulation,” *Proceedings of the 29th European Rotorcraft Forum*, Friedrichshafen, Germany, Sept. 2003.
- [32] Harrington, R. D., “Full-Scale-Tunnel Investigation of the Static-Thrust Performance of a Coaxial Helicopter Rotor,” TN 2318, NACA, March 1951.
- [33] Mineck, R. E. and Gorton, S. A., “Steady and Periodic Pressure Measurements on a Generic Helicopter Fuselage Model in the Presence of a Rotor,” TM 2000-210286, NASA, June 2000.
- [34] Kenyon, A. R. and Brown, R. E., “Wake Dynamics and Rotor-Fuselage Aerodynamic Interactions,” *Proceedings of the 63rd Annual Forum and Technology Display of the American Helicopter Society International*, Virginia Beach, V. A., May 2007.

- [35] Freeman, C. E. and Mineck, R. E., "Fuselage Surface Pressure Measurements of a Helicopter Wind-Tunnel Model With a 3.15-Meter Diameter Single Rotor," TM 80051, NASA, March 1979.
- [36] Phillips, C. and Brown, R. E., "Eulerian Simulation of the Fluid Dynamics of Helicopter Brownout," *Proceedings of the 64th Annual Forum of the American Helicopter Society*, Montréal, Canada, April 29–May 1 2008.
- [37] Miller, R. H., "Unsteady Air Loads on Helicopter Rotor Blades," *Journal of the Royal Aeronautical Society*, Vol. 68, No. 640, 1964, pp. 217–229.
- [38] Karthikeyan Duraisamy, Manikandan Ramasamy, J. D. B. J. G. L., "High Resolution Computational and Experimental Study of Hovering Rotor Tip Vortex Formation," Vol. 54, Nov. 2007.
- [39] Widnall, S. E., "The Structure and Dynamics of Vortex Filaments," *Annual Review of Fluid Mechanics*, Vol. 7, Jan. 1975, pp. 141–165.
- [40] Berselli, L. and Gabinelli, M., "On the Global Evolution of Vortex Filaments, Blobs, and Small Loops in 3D Ideal Flows," *Communications in Mathematical Physics*, Vol. 269, 2007, pp. 693–713.
- [41] Jones, H. E. and Caradonna, F. X., "Full-Potential Modeling of Blade-Vortex Interactions," TM 88355, NASA, Aug. 1986.
- [42] Fletcher, T. M. and Brown, R. E., "Main Rotor - Empennage Interaction and its Effects on Helicopter Flight Dynamics," *Proceedings of the 63rd Annual Forum and Technology Display of the American Helicopter Society International*, Virginia Beach, V. A., May 2007.
- [43] Vinod K. Lakshminarayan, Karthikeyan Duraisamy, J. D. B., "Computational Investigation of Coaxial Rotor Aerodynamics in Hover," *Proceedings of the 63rd Annual Forum and Technology Display of the American Helicopter Society International*, Virginia Beach, V. A., May 2007.

A APPENDIX

A.1 Rotorcraft Performance Characteristics

Table A.1: Performance characteristics of the isolated main rotor.

Coefficient:	Thrust	Power	Pitching Moment
Lower Rotor	6.056×10^{-3}	3.763×10^{-4}	1.272×10^{-4}
Upper Rotor	5.950×10^{-3}	3.763×10^{-4}	-1.273×10^{-4}
Main Rotor	1.201×10^{-2}	7.526×10^{-4}	0

Table A.2: Performance characteristics of the main rotor and propulsor configuration.

Coefficient:	Thrust	Power	Pitching Moment
Lower Rotor	6.194×10^{-3}	3.910×10^{-4}	7.677×10^{-5}
Upper Rotor	5.843×10^{-3}	3.738×10^{-4}	-1.824×10^{-4}
Main Rotor	1.204×10^{-2}	7.648×10^{-4}	-1.056×10^{-4}
Propulsor	2.222×10^{-4}	2.029×10^{-5}	1.052×10^{-4}

Table A.3: Performance characteristics of the full configuration.

Coefficient:	Thrust	Power	Pitching Moment
Lower Rotor	6.153×10^{-3}	4.029×10^{-4}	-3.573×10^{-4}
Upper Rotor	6.602×10^{-3}	4.310×10^{-4}	-6.345×10^{-4}
Main Rotor	1.276×10^{-2}	8.339×10^{-4}	-9.918×10^{-4}
Propulsor	1.487×10^{-4}	1.701×10^{-5}	5.761×10^{-5}

Note: The propulsor thrust, power and pitching moment coefficients given in the tables above are defined on the basis of the rotational speed of the main rotor, Ω , and main rotor radius, R .

A.2 Isolated Main Rotor

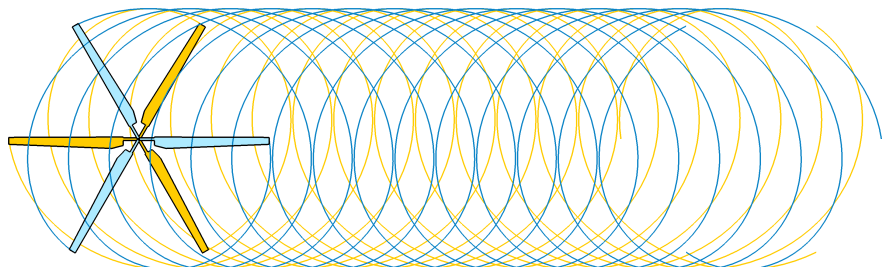


Figure A.1: Tip vortex filaments trailed by the coaxial rotor system as viewed from above. Lower rotor rotating with $\pi/3 \text{ rad}$ in advance with respect to the upper rotor.

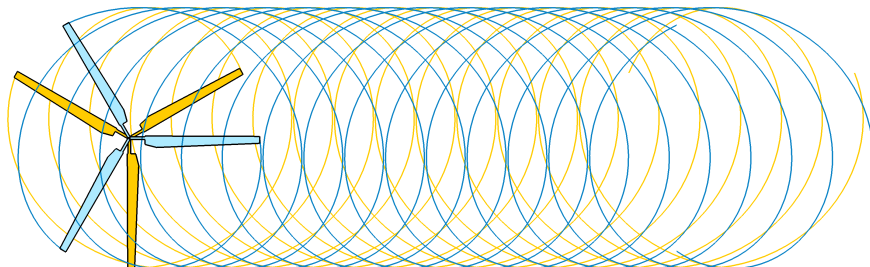


Figure A.2: Tip vortex filaments trailed by the coaxial rotor system as viewed from above. Lower rotor rotating with $\pi/2 \text{ rad}$ in advance with respect to the upper rotor.

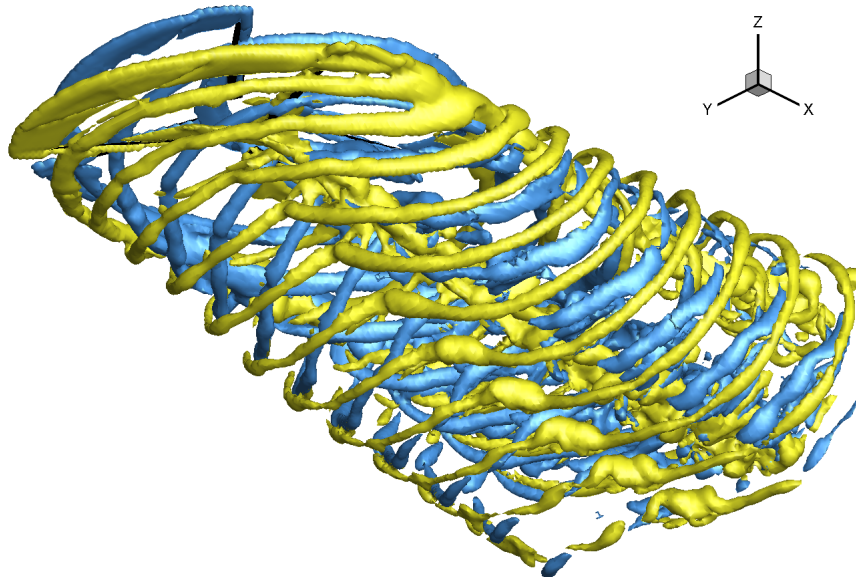


Figure A.3: Bottom view of the iso-surfaces of vorticity magnitude generated by the main rotor when operating in isolation at advance ratio $\mu = 0.15$. (Iso-surfaces from different rotors rendered separately in distinct colours.)

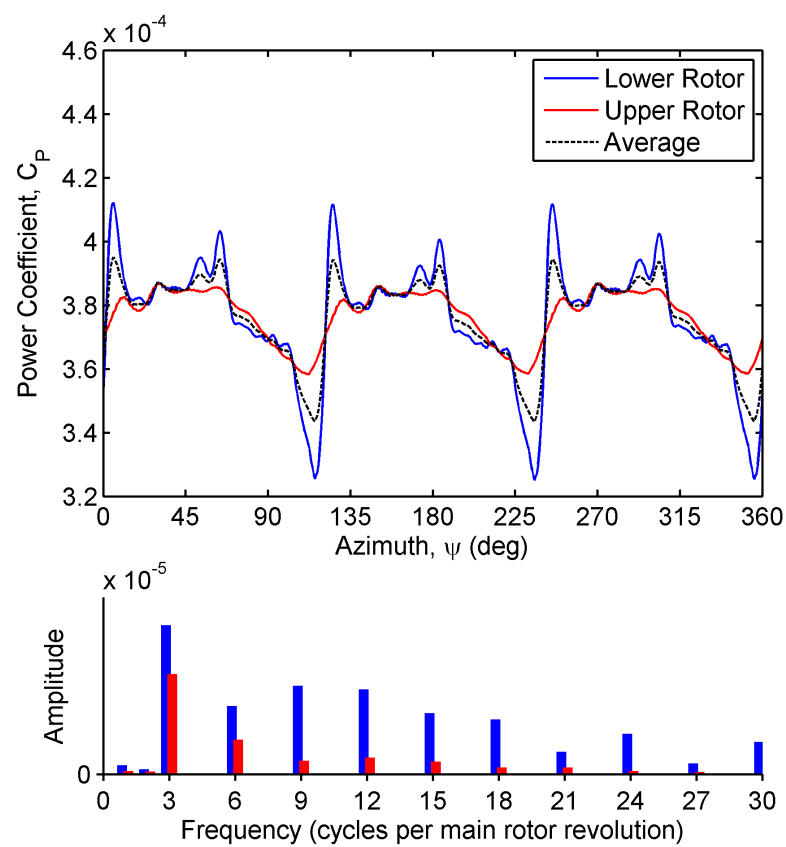


Figure A.4: Power coefficient consumed by the upper and lower rotors of the main coaxial system and correspondent frequency spectrum for the isolated main rotor.

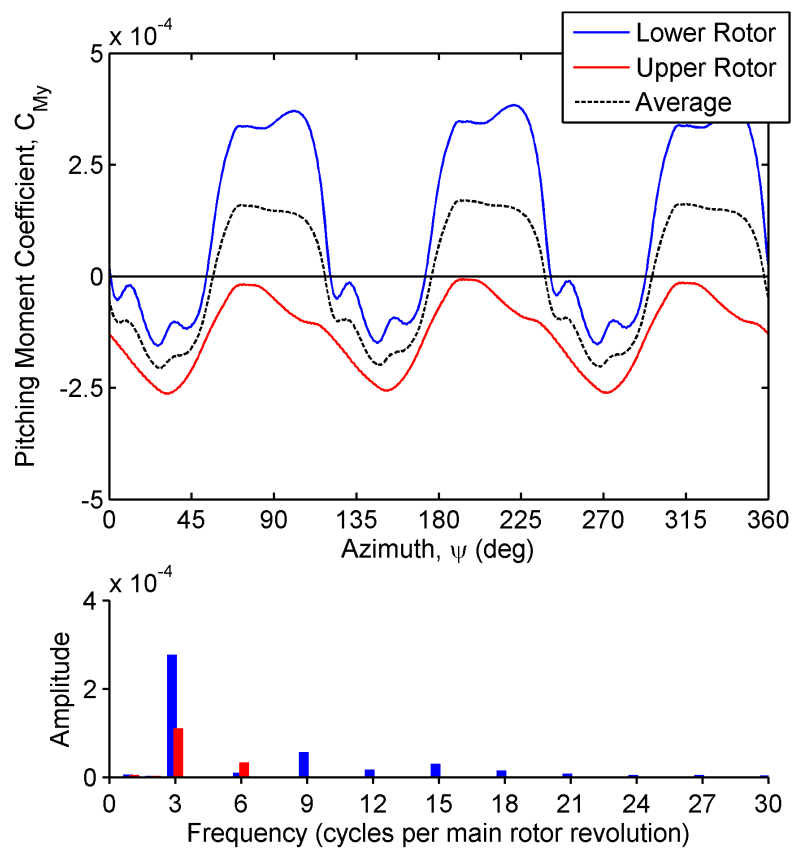


Figure A.5: Pitching moment coefficient produced by the upper and lower rotors of the main coaxial system and correspondent frequency spectrum.

A.3 Isolated Auxiliary Propulsor

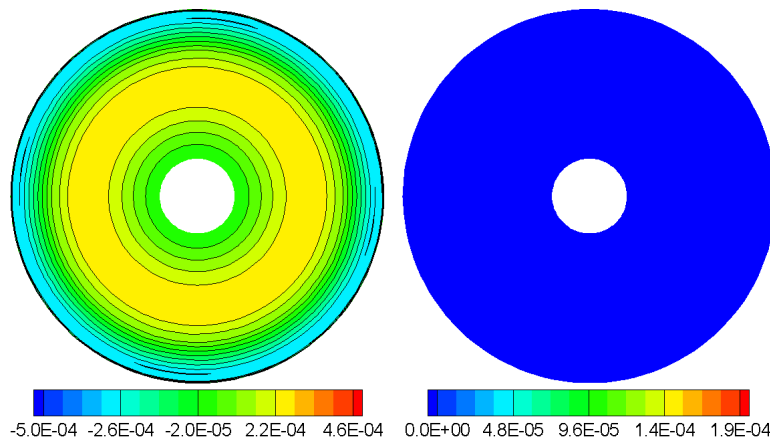


Figure A.6: Distribution of blade loading over a representative blade of the auxiliary propulsor during a complete revolution when the auxiliary propulsor is operating in isolation and producing the same thrust as when operating in the full configuration. Left: mean loading. Right: RMS fluctuation in loading.

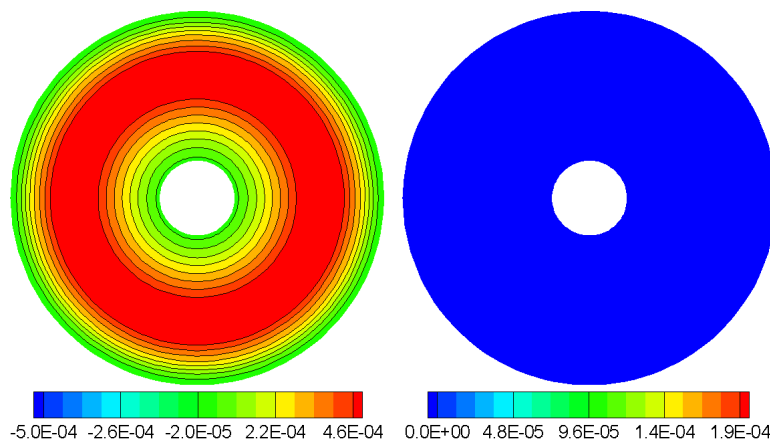


Figure A.7: Distribution of blade loading over a representative blade of the auxiliary propulsor during a complete revolution when the auxiliary propulsor is operating in isolation with the same collective pitch control as when operating in the full configuration. Left: mean loading. Right: RMS fluctuation in loading.

A.4 Main Rotor and Auxiliary Propulsor

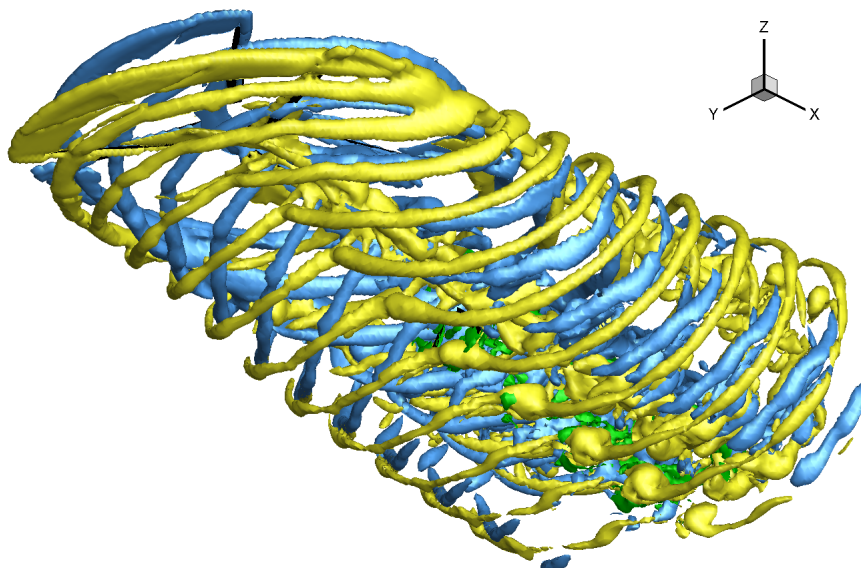


Figure A.8: Bottom view of the iso-surfaces of vorticity magnitude generated by the main rotor when operating together with the auxiliary propulsor at advance ratio $\mu = 0.15$. (Iso-surfaces from different rotors rendered separately in distinct colours.)

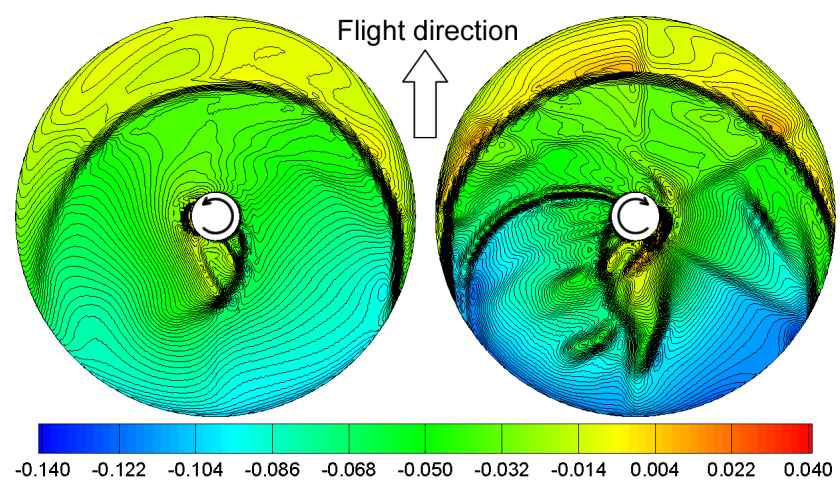


Figure A.9: Distribution of inflow over the blades of the upper and lower rotors during a complete rotor revolution for the configuration comprised of the main rotor and auxiliary propulsor. Left: upper rotor. Right: lower rotor.

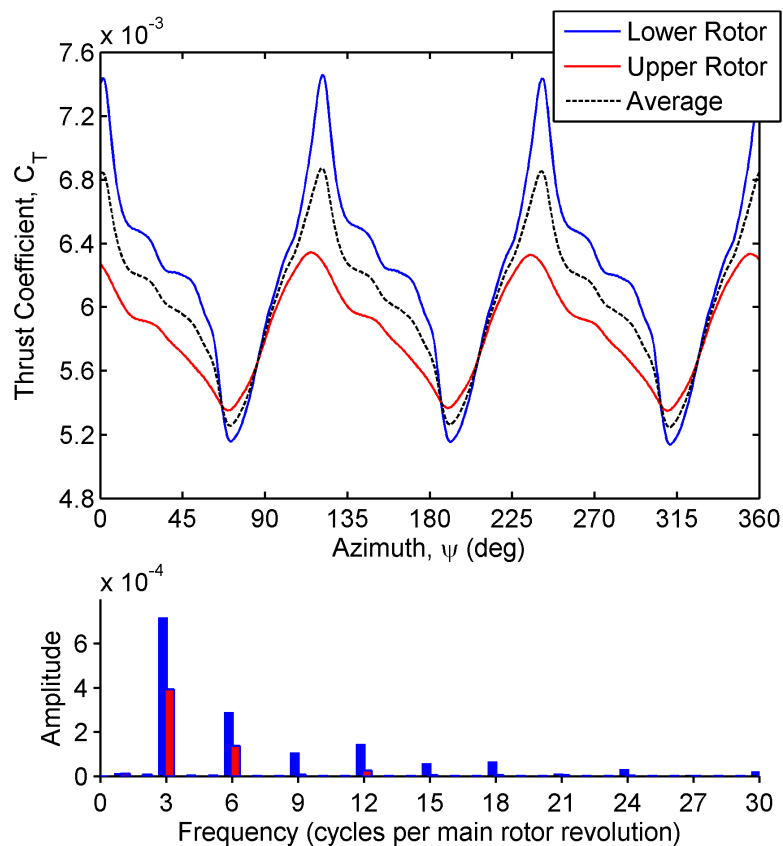


Figure A.10: Thrust coefficient generated by the upper and lower rotors and correspondent frequency spectrum for the configuration comprised of the main rotor and auxiliary propulsor.

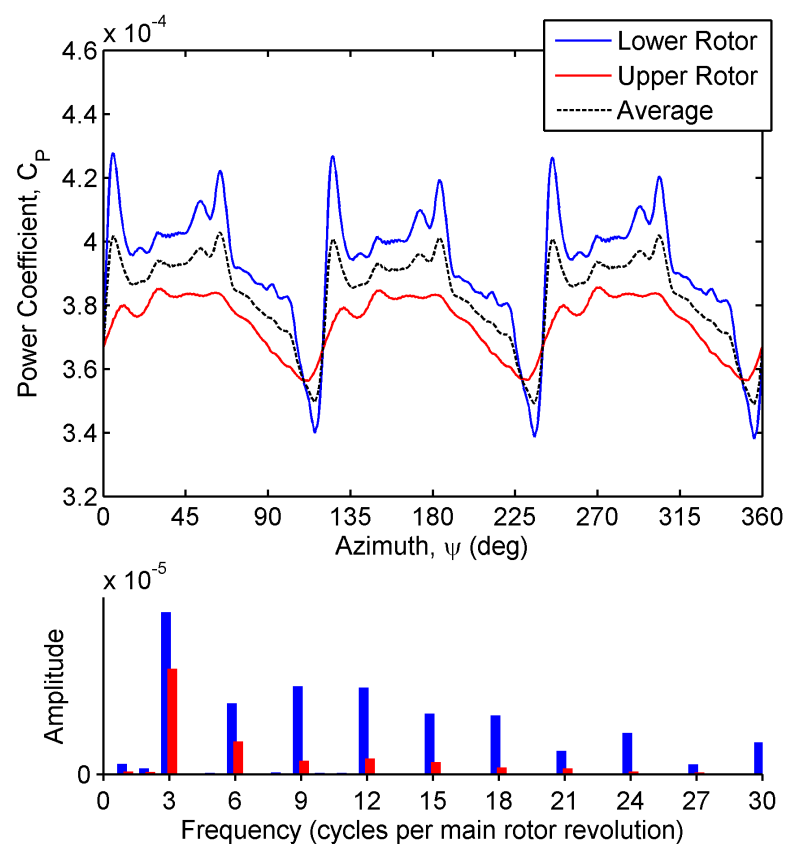


Figure A.11: Power coefficient consumed by the upper and lower rotors and correspondent frequency spectrum for the configuration comprised of the main rotor and auxiliary propulsor.

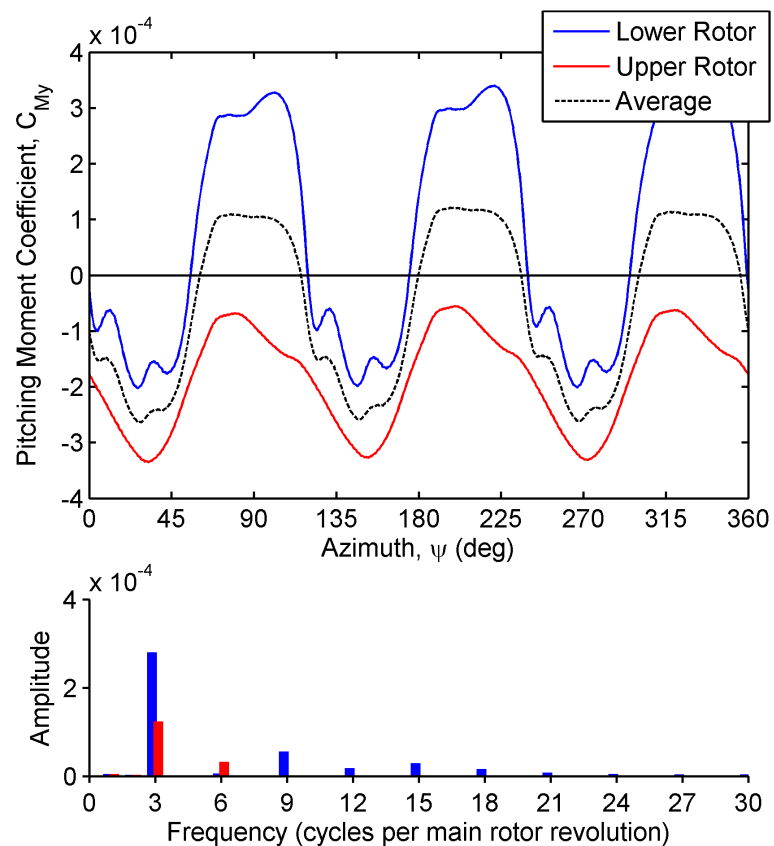


Figure A.12: Pitching moment coefficient produced by the upper and lower rotors and correspondent frequency spectrum for the configuration comprised of the main rotor and auxiliary propulsor.

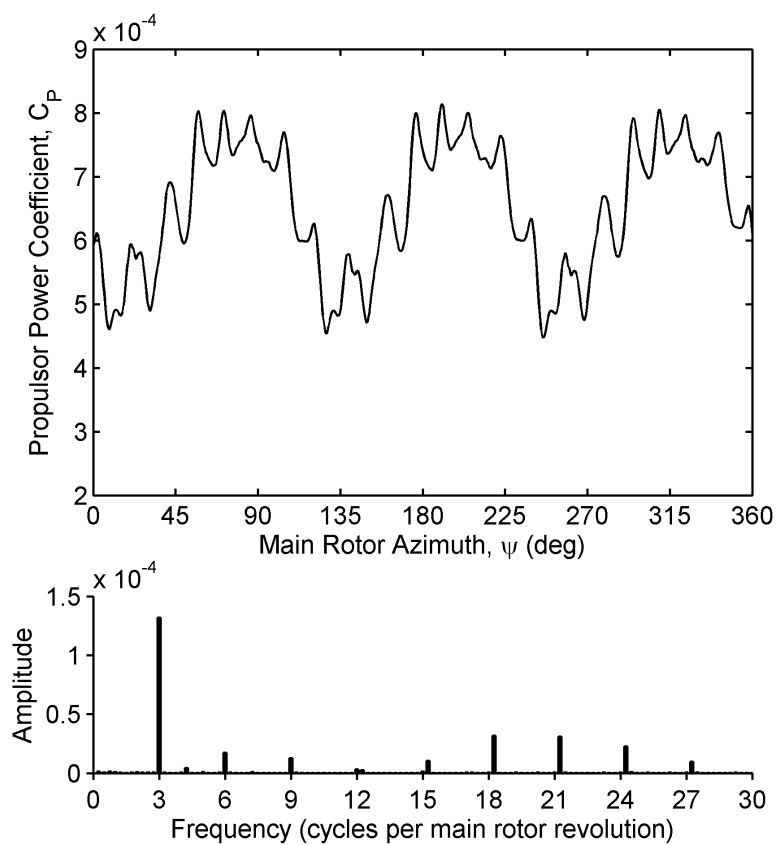


Figure A.13: Power coefficient consumed by the auxiliary propulsor over a complete main rotor revolution as a function of main rotor azimuth and respective frequency spectrum. (Power coefficient defined on the basis of the rotational speed, Ω_p , and radius, R_p , of the auxiliary propulsor.)

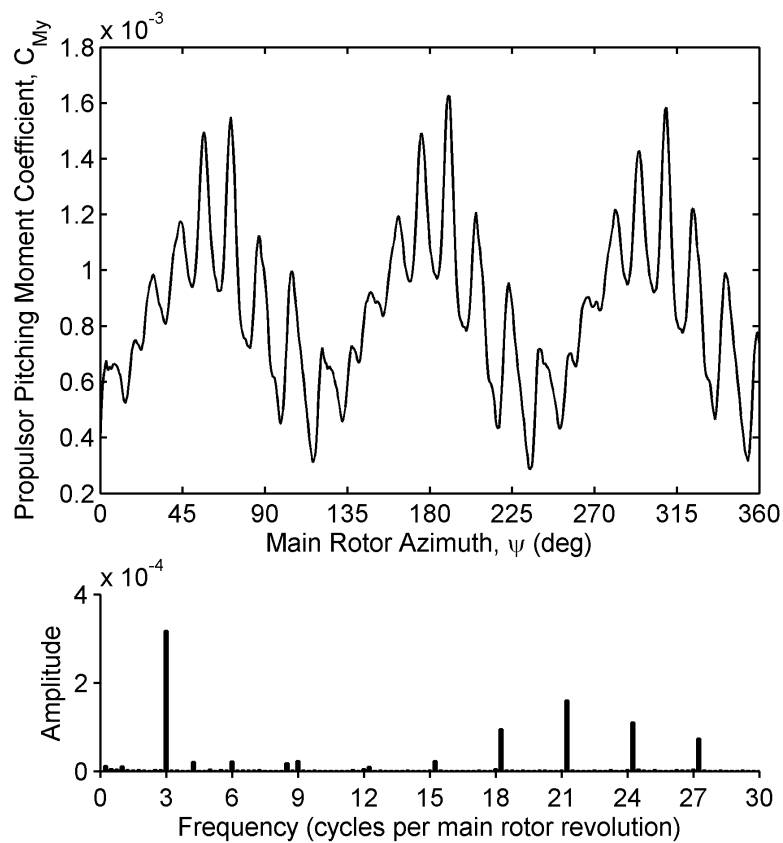


Figure A.14: Pitching moment coefficient generated by the auxiliary propulsor over a complete main rotor revolution as a function of main rotor azimuth and respective frequency spectrum. (Pitching moment coefficient defined on the basis of the rotational speed, Ω_p , and radius, R_p , of the auxiliary propulsor.)

A.5 Complete Configuration

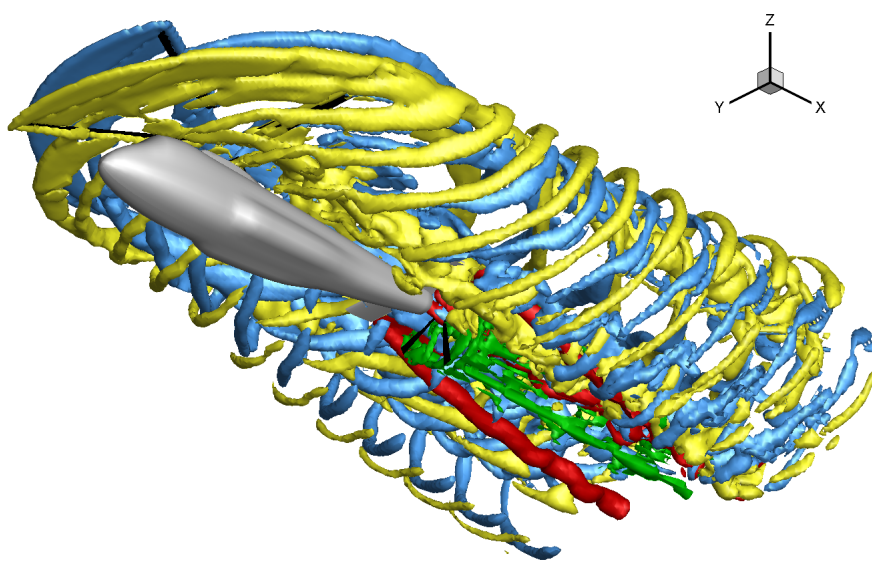


Figure A.15: Bottom view of the iso-surfaces of vorticity magnitude generated by the main rotor as part of the complete configuration at advance ratio $\mu = 0.15$. (Iso-surfaces from different rotors rendered separately in distinct colours.)

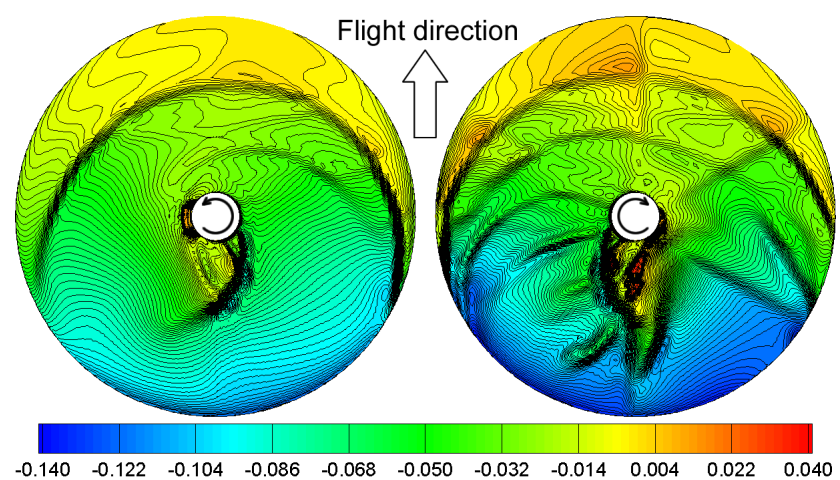


Figure A.16: Distribution of inflow over the blades of the upper and lower rotors during one rotor revolution for the complete configuration. Left: upper rotor. Right: lower rotor.

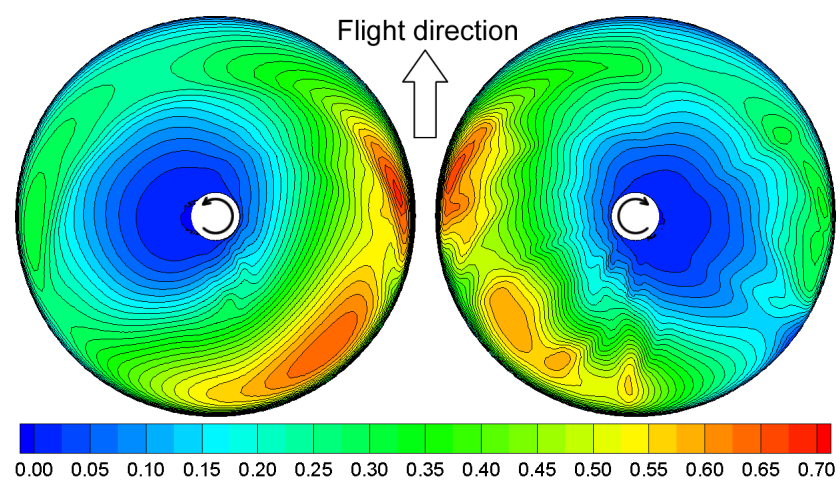


Figure A.17: Distribution of loading over the blades of the upper and lower rotors during one rotor revolution for the complete configuration. Left: upper rotor. Right: lower rotor.

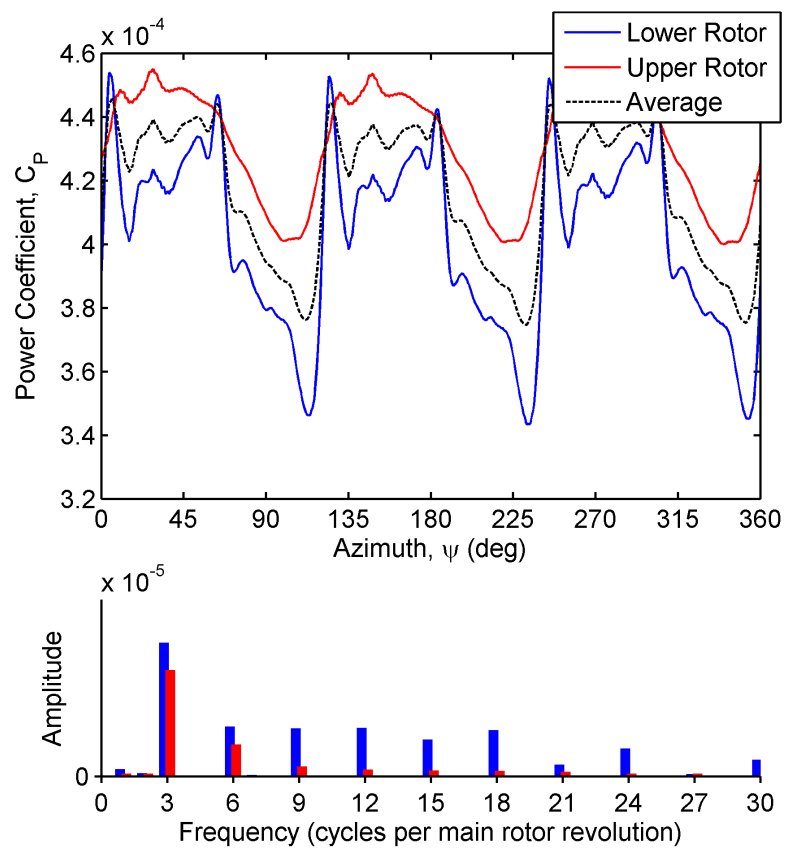


Figure A.18: Power coefficient consumed by the upper and lower rotors and correspondent frequency spectrum for the complete configuration.

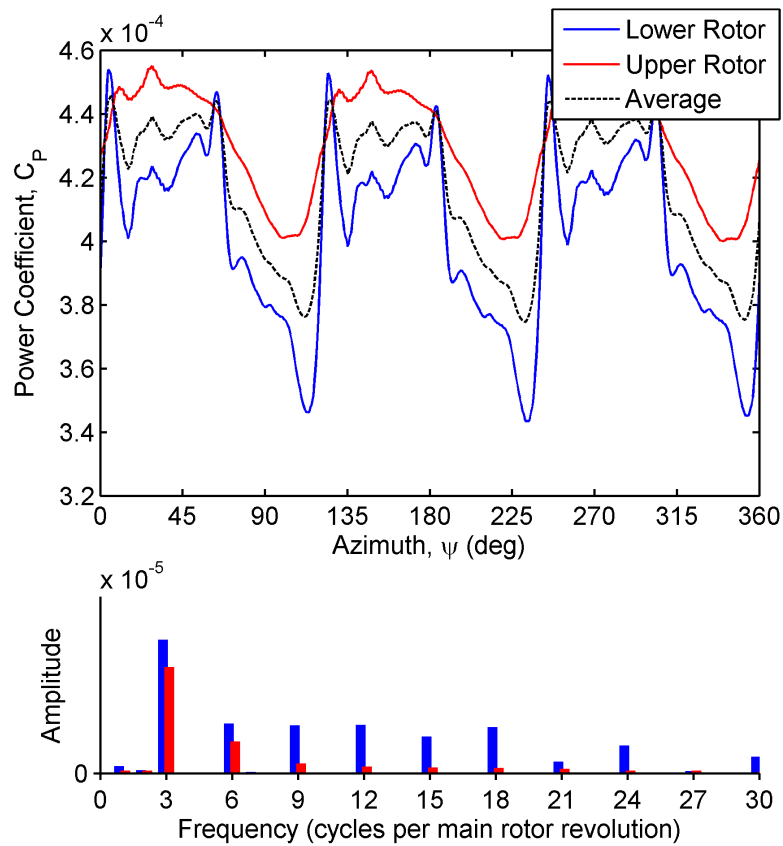


Figure A.19: Pitching moment coefficient produced by the upper and lower rotors and correspondent frequency spectrum for the complete configuration.

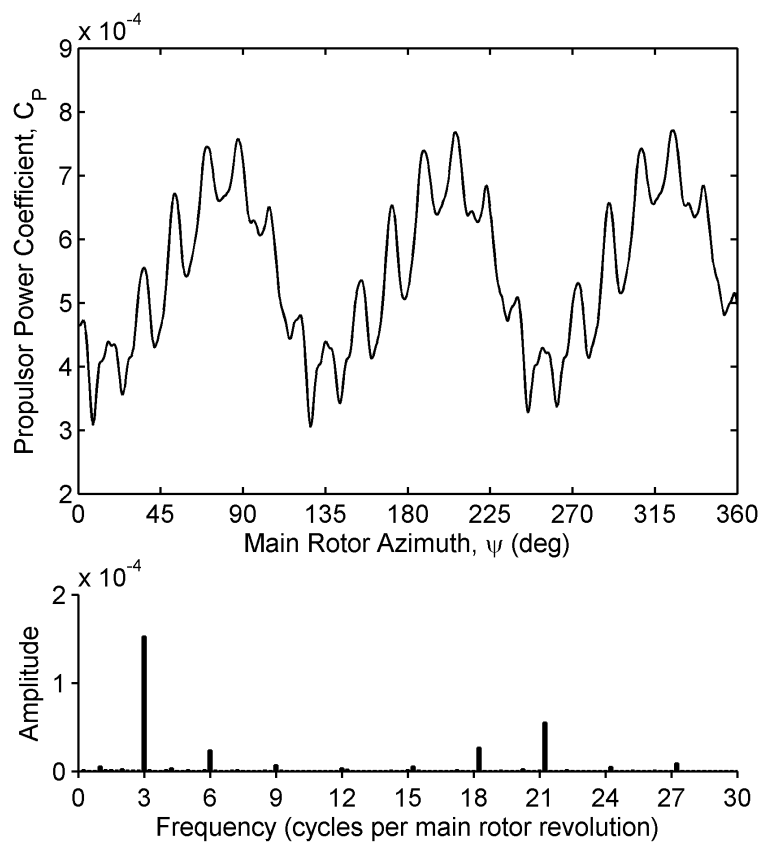


Figure A.20: Power coefficient consumed by the auxiliary propulsor over a complete main rotor revolution as a function of main rotor azimuth and respective frequency spectrum, for the complete configuration. (Power coefficient defined on the basis of the rotational speed, Ω_p , and radius, R_p , of the auxiliary propulsor.

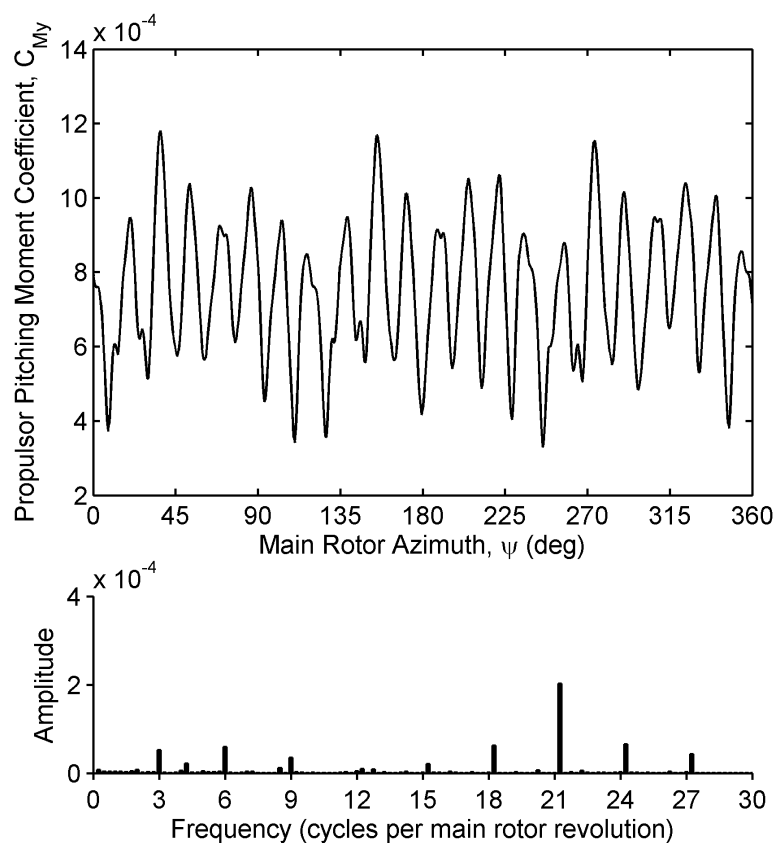


Figure A.21: Pitching moment coefficient generated by the auxiliary propulsor over a complete main rotor revolution as a function of main rotor azimuth and respective frequency spectrum for the complete configuration. (Pitching moment coefficient defined on the basis of the rotational speed, Ω_p , and radius, R_p , of the auxiliary propulsor.

A.6 Auxiliary Propulsor Wake

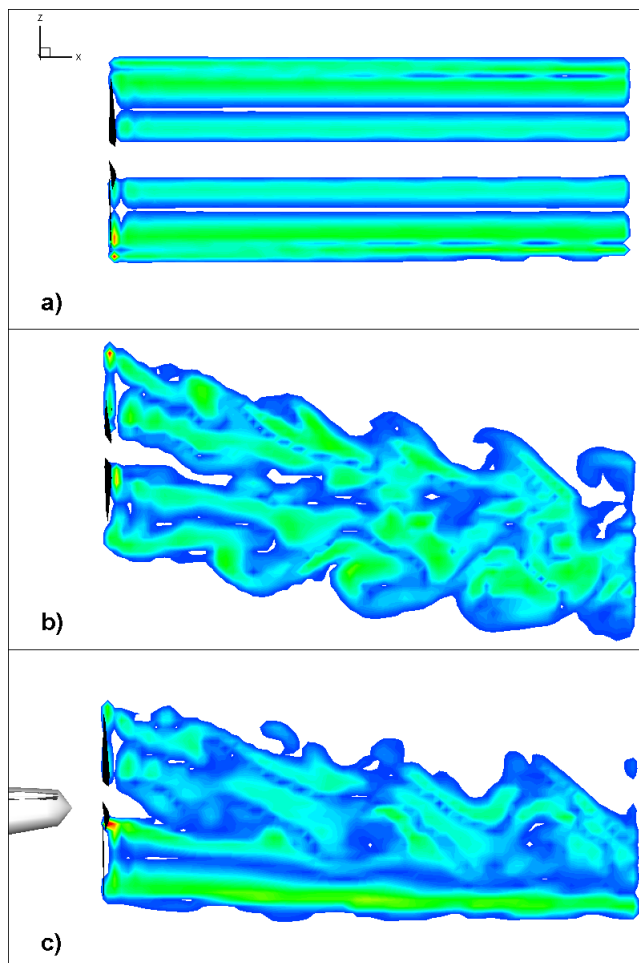


Figure A.22: Contour plot of the y -component of non-dimensional vorticity in the $x - z$ plane that is produced by the auxiliary propulsor. a) Isolated auxiliary propulsor. b) Auxiliary propulsor operating under the influence of the main rotor wake. c) Auxiliary propulsor operating under the influence of the main rotor wake, fuselage and tailplane.

A.7 Mean and Root Mean Square Decomposition

Consider the rigid auxiliary propulsor operating in isolation. It is known that the rotor aerodynamic properties are periodic in nature and that the variation of a particular property with time may be decomposed into sinusoidal functions of different frequencies. The lowest frequency that can be expected is the propulsor frequency $f_p = \Omega_p/(2\pi)$, where Ω_p is given in rad s^{-1} . However, the aerodynamic interaction with another helicopter component may reflect in that property and introduce lower frequency components. Thus the period of the variation of that property with time will be higher than the propulsor period of rotation. However, it might be beneficial to analyse the variation of this property over one propulsor revolution. In order to do that effectively the given property may be described as an average, or mean, and a RMS component. The mean property should be taken with respect to time and the RMS component represents the fluctuations of the property with respect to the mean.

Suppose that the aerodynamic property under consideration can be described as a field $F : D \rightarrow \mathbb{R}$, where the domain D is the set

$$D = \{(r, t) \in \mathbb{R}^2 | R_{p_0} \leq r \leq R_p \text{ and } t_0 \leq t < t_0 + T\}.$$

The constants R_{p_0} and R_p are the root cut-out radius and total radius of the propulsor. The time t_0 is any instant of time considered to be far enough from the initial transient response of the property. The constant T is the period of the given property and, assuming that the propulsor rotates at some fraction of the main rotor angular speed, is given by the lowest possible integer number of propulsor revolutions, N , that must be completed such that the main rotor has completed an integer number of revolutions as well. In this way, the frequency components induced by the main rotor in the propulsor are fully captured in F . Then T is given by NT_p , where $T_p = 2\pi/\Omega_p$ is the propulsor period of rotation.

The mean property is given by the field $\bar{F} : M \rightarrow \mathbb{R}$ and can be obtained by the formula:

$$\bar{F}(r, \tau) = \frac{1}{N} \sum_{i=0}^{N-1} F(r, \tau + iT_p)$$

where $0 \leq \tau < T_p$.

The RMS fluctuation of the property is the field $\hat{F} : M \rightarrow \mathbb{R}$ and is given by

$$\hat{F}(r, \tau) = \left[\frac{1}{N} \sum_{i=0}^{N-1} (\bar{F} - F(r, \tau + iT_p))^2 \right]^{\frac{1}{2}}$$